Navigating Copper-Atom-Pair Structural Effect inside Porous-Organic-Polymer Cavity for Selective Hydrogenation of Biomass Derived 5-Hydroxymethylfurfural

Chitra Sarkar,[§,⊥,Δ] Ratul Paul,[§,⊥,Δ] Subhash Chandra Shit,[§,⊥] Quang Thang Trinh,[±] Paramita Koley,[§] Bolla Srinivasa Rao,[§,⊥] Andrew M. Beale,[†] Chih-Wen Pao,[‡] Arghya Banerjee[‖,*] and John Mondal[§,⊥,*]

[§]Catalysis and Fine Chemicals Division, CSIR-Indian Institute of Chemical Technology, Uppal Road, Hyderabad-500007, India.

[⊥]Academy of Scientific and Innovative Research (AcSIR), Ghaziabad- 201002, India.

±Institute of Research and Development, Duy Tan University, 03 Quang Trung, Danang 550000, Viet Nam.

[†]Department of Chemistry, 20 Gordon Street, University College London, London, WC1H 0AJ, UK.

[‡]National Synchrotron Radiation Research Center, 101 Hsin-Ann Road, Hsinchu 30076, Taiwan.

[‖]Department of Chemical Engineering, Indian Institute of Technology, Ropar, Nangal Road, Rupnagar, Punjab, India.

[Δ]These two authors have equally contributed in this manuscript.

Corresponding Authors

*E-mail: johnmondal@iict.res.in, johncuchem@gmail.com (Mondal)

arghyab@iitrpr.ac.in (Banerjee).

Abstract: In recent times, selective-hydrogenation of biomass-derived 5-hydroxymethylfurfural (5-HMF) to produce novel difuranic polyol scaffold 2,5-dihydroxymethylfuran (DHMF) has attracted the interests of the many researchers due to its peculiar symmetrical structure as well as its wide application as a monomer for the preparation of cross-linked polyesters and polyurethane. Copper-based catalysts have been explored accountable for the selective catalytic hydrogenation however the hurdles are still associated with the strongly reducing H_2 atmosphere and oxidizing C-O bond that makes the Cu^0 and Cu^{x+} surface active species unstable, limiting the rational design of highly efficient integrated catalyst systems. To address this, herein, we built catalytic systems for 5-HMF hydrogenation with stable and balanced Cu^0 and Cu^{x+} active surface

species inside the nanocage of catechol based Porous-Organic-Polymer (POP) endowed with large surface areas, impressive stabilities, and spatial restriction inhibiting NPs aggregation. Batch reactor screening indentified that superior catalytic performance (DHMF selectivity of 98%) has been achieved with our newly designed Cu@C-POP at 150ºC temperature and 20 bar H_2 pressure, which was also higher than that of other reported copper catalysts. Comprehensive characterizations understanding with H_2-TPR and XPS study revealed that substantially boosted activity is induced by the presence of bulk CuO_x phase and atomically dispersed Cu species incorporating isolated Cu ions, which are further confirmed through the positive binding energy shift of Cu-$2p_{3/2}$ XPS spectra (~0.4eV). The Cu environment in our catalytic systems comprises predominantly square planar (well probably Jahn-Teller distorted Oh) which we gleaned from the EXAFS analysis featuring two adjacent copper atoms with the valence state in between of 0 and +2 as validated by XANES absorption edge positions. EXAFS studies further revealed a lowering of Cu coordination number for the most active Cu@C-POP-**B** catalyst suggesting the presence of metal vacancies. Density Functional Theory calculations showed that the presence of Cu metal vacancies stabilized the reaction intermediates formed during 5-HMF hydrogenation and decreased the hydrogenation barriers resulting in an enhanced catalytic activity of the Cu@C-POP-**B** catalyst.

Keywords: *Porous-Organic-Polymer (POP), Biomass, 5-Hydroxymethylfurfural (HMF), Cu-cooperative effect, Cu^0-Cu^{x+} dual atom pair species*

Introduction:

The limited stock of fossil fuels and growing concern about global climate change played a crucial role behind the wisdom to discover the alternative energy sources, such as biomass derived carbohydrates.[1,2,3] Bio-refinery is a widely advanced concept to transform the biomass derived oxygenates to generate biofuel.[4,5,6] 5-hydroxymethylfurfural (5-HMF) is a platform chemical of lignocelluloses valorization. Among the hydrogenated products including 2,5-dihydroxymethylfuran (DHMF), 2,5-dihydroxymethyltetrahydrofuran (DHMTHF), 2,5-dimethylfuran (DMF), 2,5-dimethyltetrahydrofuran (DMTHF) *etc*. ,DHMF had been attracted significantly due to tremendous application in the production of resin, ethers, artificial fibers and as an important intermediate in drug synthesis.[7] The trend of using noble metal catalyst for HMF hydrogenation for past decades, is the major restraint to industrial application, such as Mitra *et*

al. demonstrated the diverse reactivity of HMF over Pd/C catalyst in presence of biomass derived additives.[8] The detailed description of the effects of metal, support, solution phase acidity, and the solvent over Ru, Pd, and Pt supported catalysts in monophasic and biphasic reactor for 5-HMF to DHMTHF hydrogenation was also extensively studied.[9] Satsuma *et al*. utilized the basic principal of acid- base property of various metal oxide support with Au metal for selective hydrogenation of 5-HMF to DHMF.[10] In recent years, tremendous efforts have been focused in designing and exploring Cu-based heterogeneous catalysts considering both balanced and stable Cu^0 and Cu^{x+} surface species play decisive role to the activity.[11] Sun *et.al* have observed that the addition of alkali/alkaline earth metals could drastically enhance the catalytic activity for hydrogenation of 5-HMF to DHMF at low temperatures, attributing to the synergetic effects between the additives and copper.[12] MOF-derived bimetallic nickel-copper catalyst has been designed by Xu and co-workers for catalytic selective hydrogenation of 5-HMF in water.[13] Similarly, mineral and metal-organic-framework (MOF) derived Cu-ZnO, CuNPs@ZIF-8 catalysts are also reported for highly selective hydrogenation of 5-HMF with ~99% of DHMF yield.[14,15] Zhang *et.al* have adopted controlled thermolysis technique of Cu-BTC-MOF to attain highly selective hydrogenation of 5-HMF.[16] However, despite these extensive studies the hurdles of these conventional copper-based catalysts are still associated with the strongly reducing H_2 atmosphere and oxidizing C-O bond make the Cu^0 and Cu^{x+} surface species unstable, thereby triggering catalyst deactivation.[17]

So, the discovery of Cu-supported catalysts with stable structures and coexisting Cu^0 and Cu^{x+} active species for selective production of DHMF from 5-HMF, is highly desirable but still a challenging task for the researchers. In the recent years, intriguing interest is growing to employ POP (Porous-Organic-Polymer) with versatile functionalities as molecular support in heterogeneous catalysis compared to other conventional supports, owing to their mechanically stable rigid covalent framework with tunable pore structure, low skeleton density, specifically huge surface area, controllable compositions, and powerful nanoconfinement effects for atomically dispersion of the metal NPs to prevent further agglomeration and sintering.[18,19,20] The major challenge in realizing the strategic design of POPs with customized functionalities by accommodating the building blocks with ultimate accuracy and precision is to recognize the appropriate monomers. In pursue of our viewpoint herein, we have accomplished a truly cost effective fruitful synthesis of -OH group functionalized catechol based POP (C-POP) *via* Friedel-

Craft condensation-polymerization reaction between catechol and dimethoxymethane, using $FeCl_3$ as promoter. Further simple and efficient modification has been achieved to fabricate atomically dispersed Cu-NPs on the POP support inside or outside of the cavity with stable and balanced Cu^0 and Cu^{x+} active surface species to furnish catalytic systems. We chose the selective hydrogenation of biomass derived 5-HMF as a platform molecule as a probe reaction to investigate the catalytic efficiency and stability of the Cu-POP based catalytic systems.

EXPERIMENTAL SECTION:

Materials and Methods:

Catechol, anhydrous ferric chloride ($FeCl_3$), dimethoxymethane, copper (II) acetate monohydrate ($Cu(OAc)_2.H_2O$), copper(II) chloride dihydrate($CuCl_2$, $2H_2O$) were purchased from Sigma-Aldrich and used in reaction without further purification. All the solvents (dichloroethane, methanol) were dried before using in the reaction.

Computational Methods:

Spin polarised density functional theory calculations were performed using the Vienna ab-initio simulation package (VASP) as developed at the Fakultat fur Physik of Universitat Wien.[21] To account for the weak long-range van der Waals interactions in adsorption, the vdw-DF functional[22] in the generalized gradient approximation (GGA) was employed in all our calculations, with a plane wave basis set having a cutoff kinetic energy of 450 eV. The vdW-DF functional has been shown to predict CO_2 and CO binding on the Cu surface reasonably well.[23] XPS, EXAFS and TEM analysis of the catalysts revealed the presence of CuO as the dominant species on both the catalyst surfaces. The most stable CuO(111) facet was chosen for our calculations. The GGA formulation however, severely under estimates the electronic and magnetic properties of metal oxides. The DFT+U formalism as proposed by Duadurev[24] was employed with a U value of 4.5 eV with a bulk like magnetic ordering[25] to accurately predict surface catalysed reactions pathways and energetics on the CuO surface. The CuO(111) surface was modelled as a 5 layer (4x2) unit cell with optimised lattice constants of a = 4.61 Å, b = 3.68 Å and c =5.25 Å, $\beta = 99.5°$. The Brillouin zone was sampled with a 3 x 3 x 1 Monkhorst Pack grid, and a tetrahedron method of smearing having width of 0.2 eV was employed. Geometry

optimisation was done using a conjugate gradient algorithm with a force convergence criteria of 0.05 eV/ Å. An interslab spacing of 15 Å was used to minimise the interslab interactions. The climbing image Nudged Elastic Band method[26] was employed for estimation of the transition states. 4-6 images were used in the NEB and the forces minimised to 0.05 eV/ Å. The NEB image closest to the transition state was further optimized using the quasi-Newton algorithm, and a vibrational frequency analysis was done with a displacement criteria of 0.01 Å to confirm the transition state.

Synthesis of Catechol based Porous-Organic-Polymer (C-POP):

Porous-Organic-Polymer (POP) nanospheres were developed by anhydrous $FeCl_3$ assisted polymerization reaction accompanied by dimethoxymethane and catechol, with slight modification of previous report.[27] At first 0.2 g of catechol and 0.6 g $FeCl_3$ was stirred in 15 ml dichloroethane in 50 ml two neck round bottom flask at refluxing condition. Dimethoxymethane was charged into the reaction mixture to initiate the polymerization process and reaction was continued to 20h. The solid dark color residue was collected by centrifugation and washed with copious amount of methanol, than subjected to soxhlet apparatus for 30 h with refluxing methanol. Ultimately obtained the dark brown solid was dried and denoted as C-POP.

Synthesis of Cu@C-POP-**A and** Cu@C-POP-**B:**

In a typical synthetic procedure, 150 mg C-POP was dispersed in 30 ml water followed by addition of 50 mg $Cu(OAc)_2.H_2O$(0.2 mmol) and continued stirring at 80 °C.After 14h, 100 mg ammonium formate was charged into the reaction mixture with constant stirring for 1h.The resulting mixture was then transferred into a Teflon lined autoclave for 6h at 160 °C temperature. The black residue was washed thoroughly with MeOH and acetone to furnish Cu@C-POP-**A** sample. For Cu@C-POP-**B**, 200 mg C-POP was charged in a 100 ml round bottom flask followed by dispersion in 30 ml water through sonication for ~1h. The metal precursor ($CuCl_2$, $2H_2O$) ~70mg was added to the previous POP solution and stirred for 2h at room temperature to ensure the incorporation metal particles on microporous network. Furthermore, 2 ml ice cooled solution of $NaBH_4$ (100 mg in 2 ml H_2O) was added to the resulting mixture and continued to stir for another 1h to reduce metal particles. Finally, the obtained material was collected by

centrifugation technique subsequently washing with MeOH to drain off unreacted metal particles and dried overnight to obtain Cu@C-POP-**B** catalyst.

Catalytic activity for the Selective Hydrogenation of Biomass Derived 5-Hydroxymethylfurfural:

Selective hydrogenation of HMF to DHMF were performed in a 100 ml Parr autoclave (high pressure reactor), equipped with a magnetic stirrer and accompanied by inbuilt pressure gauge set up with certain pressure range (0-12MPa) and temperature (max=573K). In a typical catalytic run, HMF (0.126g, 1mmol), catalyst (0.03g) along with 30 ml ethanol were charged into the reactor. To remove dissolved oxygen or air the reactor was then sealed and evacuated by vacuum pump for 15 min at room temperature. The pressure of the reactor was kept fixed at 20 bars after continuous purging the H_2 gas at least for ten times. Furthermore, the temperature of the reaction mixture was kept fixed at 150 ^oC under the continuous stirring of 1000 rpm. Finally, when the reaction was completed the reactor was cooled down to room temperature by releasing the pressure carefully. Furthermore, catalyst was separated from the reaction mixture through centrifugation in order to analyze the reaction mixture by gas chromatography (GC) with an Agilent GC7890B gas chromatograph provided with flame ionization detectors and SE-54 capillary column (30 m×0.32mm×1.0 μm). All the liquid products were detected with respect to internal standard (anisole) in comparison with known standards having a standard deviation less than 2%.

RESULTS AND DISCUSSIONS:

Catalyst Synthesis and Characterization:

We present the schematic procedure for the synthesis of catechol functionalized POP (C-POP) by $FeCl_3$ assisted template free Friedel-Crafts condensation polymerization between catechol and dimethoxymethane and subsequent introduction of copper NPs inside the POP framework cavity in Fig. 1a (see Methods). We have chosen catechol as a monomeric unit because of its various advantages, such as the aromatic ring of catechol possesses π-π interaction between the two adjacent catechol units, which lead to maximise the cohesive properties, thus facilitates the attachment with the aromatic compounds.[28] Secondly, prominent H-bonding interaction of the ortho-dihydroxy functional group of catechol enhances the adsorption on the polar groups (N, O

etc) dominated reactant surface.[29] Moreover, cation- π interaction promotes the adherence of catechol over the aromatic as well as cation rich surface.[30] Furthermore, chelating property of catechol with various metal ions(Cu^{2+}, Zn^{2+}, Mn^{2+},Fe^{2+}, V^{3+}, Ti^{3+}, and Ti^{4+}) are appeared to be an unique strategy to construct self-healing hydrogels, pH-responsive drug carrier, soft actuators, and mechanically reinforced polymeric fibers. The abovementioned properties became silent to some extent in case of phenol containing one hydroxyl group. So, we selected catechol as monomeric unit to furnish C-POP material by $FeCl_3$ assisted template free Friedel-Crafts condensation polymerization.[31] Upon mixing the monomer (catechol) and a certain equivalent of cross-linking agent (dimethoxymethane) in 1,2-dichloroethane solvent, with stoichiometric amount of anhydrous $FeCl_3$ as catalyst under refluxing conditions afforded powder-like materials catechol functionalized POP (C-POP) which are insoluble in common organic solvents. It is noteworthy to mention that template free Friedel-Crafts (FC) alkylation technique comprises some additional advantages including highly cost-effective, very much effortless one-step synthetic strategy and reaction also engages in "knitting" various organic building blocks by a simple external cross-linker for the construction of porous organic frameworks.[32] With such a hydroxyl functional group enriched POP framework (C-POP) in our hand, we are much more passionate to reveal its effectiveness toward catalytic applications by metalation of the Cu-salts followed by liquid phase reduction. As proof of principle, we have selected to react with Cu species, in water afforded black solids after solvothermal reduction by $HCOONH_4$ and $NaBH_4$ (hereafter abbreviated as Cu@C-POP-**A** and Cu@C-POP-**B**, respectively). The absence of residual Fe confirmed by AAS(Atomic Absorption Spectroscopy) analysis, which clearly stated the Fe content below 2 ppm level for the both catalyst. Moreover, inductively coupled plasma optical emission spectrometry (ICP-OES) analysis reveals the Cu content in Cu@C-POP-**A** and Cu@C-POP-**B** are 1.35, and 1.63 $mmolg^{-1}$, respectively. As a representative material, as-synthesized C-POP was exemplified methodically with the detailed characterization results provided here. Thermogravimetric (TG) analysis of parent C-POP was performed in N_2 atmosphere to evaluate thermal stability and existence of trapped guest molecules inside the porous framework (Fig. S1). Initial weight (6mg) loss before below 100 °C is observed in the TGA curve, which is probably due to exclusion of intercalated water as well as trapped organic molecules from the organic framework. Upon constant heating, the C-POP material was stable until 310 °C temperature, indicative of its good thermal stability and after that the we could

clearly notice that a steady weight loss took place, which could be attributed to the release of free hydroxyl group and burning of porous skeleton along with C-C bond cleavage.[33]

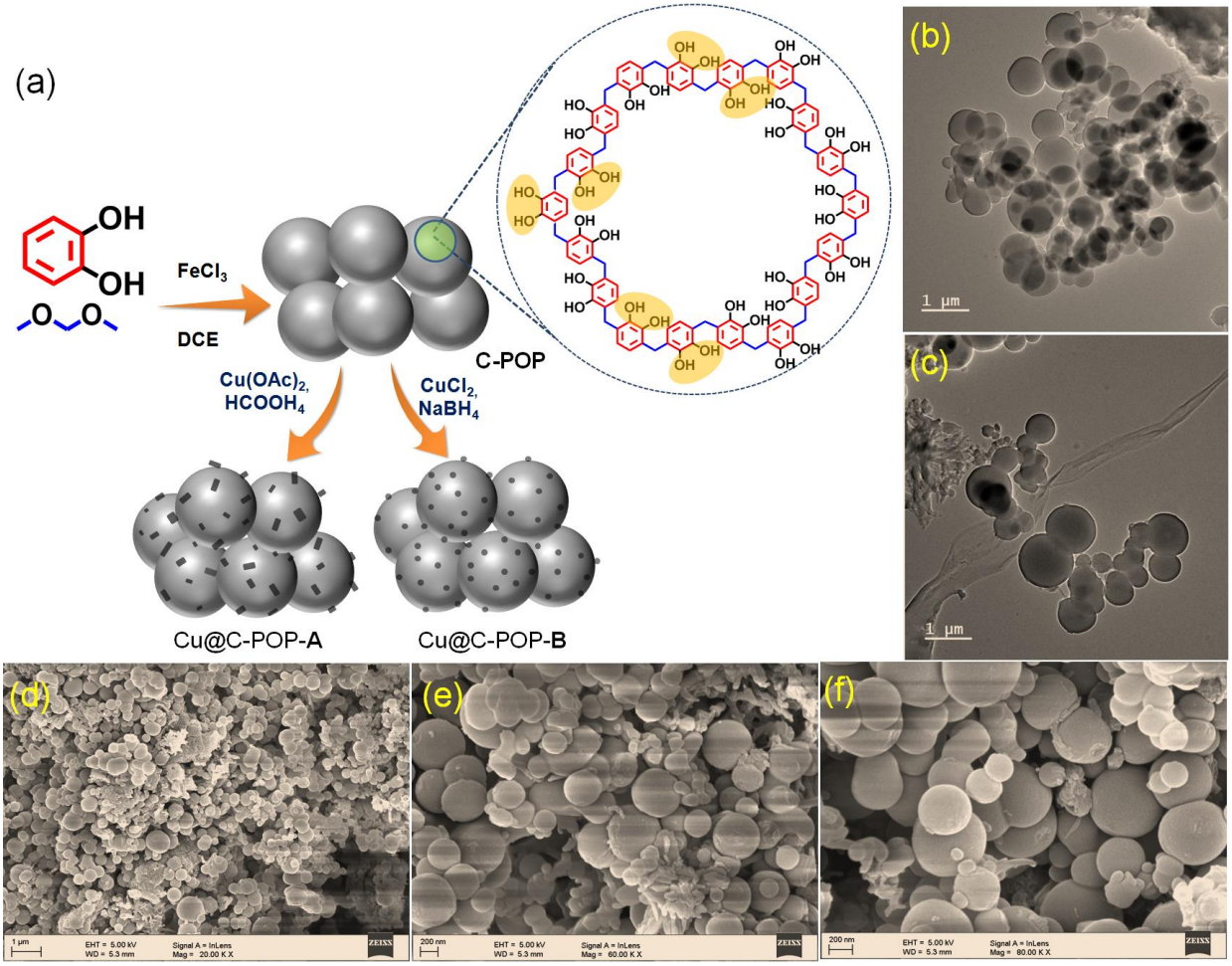

Fig. 1: (a) Schematic Illustration Showing the Synthetic Strategy of as-synthesized catechol functionalized POP (C-POP), Cu@C-POP-**A** and Cu@C-POP-**B**, respectively; TEM (b and c) and FE-SEM (d, e and f) images of C-POP.

Structural insight details of this as-synthesized C-POP material has been examined with the transmission electron microscopy (TEM) as well as Field emission scanning electron microscopy (FE-SEM) analysis. As shown in the Fig.1b and 1c, C-POP exhibits specific uniform nanosphere morphology having diameter in the range of ~0.2-1.1 µm. Several reports are already published regarding the metal chelates formation with catechol functionality in aerobic condition. There is a certain possibility of complexation of catechol with Fe^{+3} during $FeCl_3$ assisted Friedel-Crafts condensation polymerization, which promotes auto oxidation of catechol. Thus, the formation of numerous metal-catecholate functionality is initiated in order to prevent speedy agglomerates

without catechol. It was supposed that under prolong reaction condition (20h) minimum surface energy principal modulate the spherical configuration of porous organic polymer. Molecular entanglements as well as intermolecular forces between the catechol moieties such as hydrophobic interaction, H-bonding are believed to be the key factors to govern the specific uniform nanosphere formation. Similar finding was reported recently, which clearly demonstrated the genesis of CaP nanoparticles driven raspberry-like spheres coordinated with catechol.[34] It is worth pointing out that a unique overlap among the nanospheres was observed indicative of interactions among hydroxyl groups in C-POP layers (Fig. 1b and 1c). Density functional studies revealed a strong electrostatic interaction (H- bonding) between the hydrogen and oxygen atom (of the OH group) of adjacent catechol moieties which stabilised the C-POP structure by 33 kJ per OH group (Fig. S2).Although the lower magnification FE-SEM image Fig. 1d reveals the spheres morphology with some random arrangement of the as-synthesized sample, but on closer inspection we can observe the distinct nanospheres shape of -OH functionalized POP had the diameter of about ~89-635 nm (Fig.1e and 1f), with the very smooth external surface in nature. Lower magnification FE-SEM images of the both Cu@C-POP systems reveal the formation of spheres in the range of 0.11-0.49 μm along with presence of some cotton like morphology during agglomeration, provided on Fig. S3. Although the higher magnification FE-SEM image demonstrates the relative homogeneous organization of nanospheres for Cu@C-POP-**B** in stark contrast with randomly distributed sphere shapes for Cu@C-POP-**A**. The elemental distribution of Cu on the C-POP nanospheres of the very specific selected area obtained from the FE-SEM image was established by energy-dispersive X-ray spectroscopy (EDX) (Fig. S5), which indicates the abundance of each individual element present and also quantified in wt% fashion. The wide angle powder X-ray diffraction (PXRD) of the as-synthesized C-POP (Fig. S6) showed the broad peaks appeared at 2θ= 25° and 44°, respectively, attributed to the presence of C(002) and (101) planes.[35] The main peaks centered at 2θ values 43.4°, 50.4° and 74.0° for Cu@C-POP-**A** (Fig. S7), which could be indexed to (111), (200) and (220) crystalline reflections, represents the face-centered cubic (*fcc*) lattice arrangement of Cu^0-NPs (JCPDS card no. 04-0836).[36] In strong contrast, distinct reflection patterns is noticed from the PXRD spectrum of Cu@C-POP-**B** (Fig. S7) at 2θ= 29.6°, 36.3°, 42.2°, 61.5°, 73.5° and 77.3°, respectively, could be assigned to the (110), (111), (200), (220), (311) and (222) crystalline planes of Cu_2O phase after proper indexing (JCPDS NO. 65–3288).[37] Formation of

pure Cu nanoparticles is troublesome process due to the spontaneous surface oxidation in air, aqueous solutions and polar solvents. Most importantly, the increase in surface energy in Cu nano-sized arrangement and comparatively small Cu^0/Cu^{2+} redox potential (+0.34 V) induces oxidation of Cu.[38] Several reports confirmed the presence of Cu_2O during the Cu nanoparticle formation by $NaBH_4$ as reducing agent, which is followed for the synthesis of Cu@C-POP-**B** catalyst.[39] Interestingly, Chong *et al.* described that the presence of CO & H_2 have the ability to eliminate the air oxidation Cu.[40] For Cu@C-POP-**B** catalyst, high temperature (160 °C) reduction with ammonium formate may lead to the generation of CO & H_2, thus prevent the oxidation of Cu & zero valent Cu nanoparticles formed.

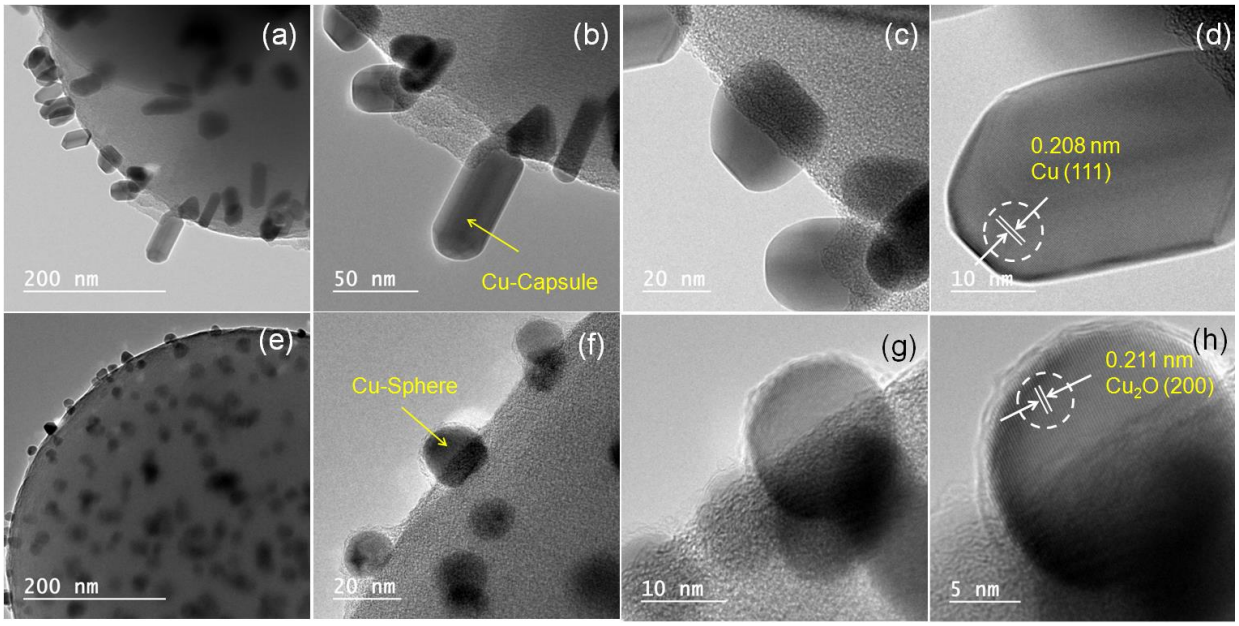

Fig. 2: TEM images of Cu@C-POP-**A** (a, b and c) and Cu@C-POP-**B** (e, f and g). HR-TEM images with corresponding crystalline lattice fringes of Cu@C-POP-**A** (d) and Cu@C-POP-**B** (h).

Electron microscopic analyses:

The significant morphological evolution was presented in the TEM images (Fig. 2), depicting the insertion of smaller copper NPs on the porous-organic-polymer network for Cu@C-POP-**B** in homogeneous fashion rather than random distribution of the Cu NPs for Cu@C-POP-**A**. As shown on the Fig. 2a, the capsules like Cu-NPs are randomly placed over external C-POP nanosphere surface. On the closer view of the TEM image (Fig. 2a) reveals the presence of irregular sphere (34.91 nm) along with cylinder consisting hemispherical ends ranging from (height=77.78nm, width=33.16) to (height=26.41, width=17.18). Fig. 2b and c also provide

visual impression about the half exposed Cu-NPs on the spherical POP surface. A clear TEM image of an individual Cu-capsule with 21.58 nm width was presented in Fig. 2d. The HR-TEM image (Fig. 2d) demonstrates the emergence of lattice fringe having d spacing of about 0.208 nm, consequent to the (111) crystalline reflection plane in face-centered cubic (*fcc*) arrangement of the individual Cu^0-NPs, is in good agreement with the PXRD result.[39] The microscopically illustration of Cu@C-POP-**B** distinctly specify random location of spherical NPs over C-POP surface have size distribution of about 9.5-27 nm (Fig. 2e) intertwined with carbonaceous network. Some crystalline particles were agglomerated to form bigger nanograins of ~54 nm diameter range. The pictorial representation of average irregularly shaped copper particles within the range of ~12-24 nm are tightly wrapped inside the porous layer was shown in Fig. 2f and g. The above mentioned layer, which is able to allocate the copper NPs inside the pores of parent porous organic framework was about 1.7 nm thick and prevent the aggregation and detachment of NPs in larger extent, is the key feature for enhancement in catalytic activity. Herein, we have observed that the corresponding interplanar *d* spacing of the lattice was 0.211 nm matched unambiguously with the (200) lattice plane of Cu_2O species.[37]

The STEM images of the two materials Cu@C-POP-**A** and Cu@C-POP-**B** (Fig. 3a and b) comprises some structural resemblance with the previous TEM images providing capsule and sphere like shape of anchored Cu particles on the C-POP surface. Additionally, we have also inspected the elemental distribution with the corresponding elemental mapping analysis (Fig. 3), which revealed that Cu (blue) atoms are nearly distributed at the same location of C (green) atoms accompanying the O (yellow) atoms, from which we can imagine some important idea regarding the precise atomic configuration of the active sites.

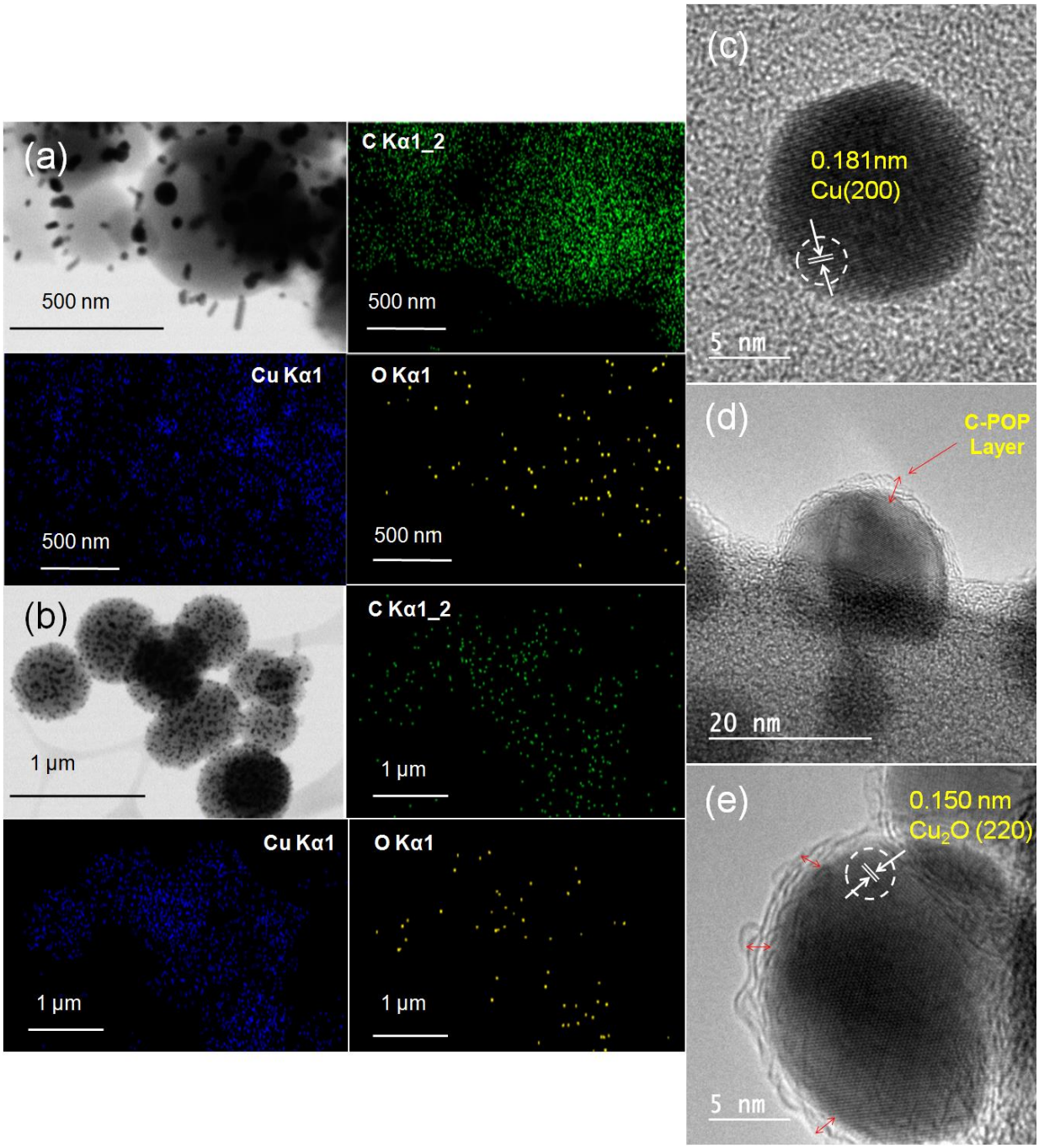

Fig. 3: STEM images of Cu@C-POP-**A** (a) and Cu@C-POP-**B** (b) with the respective elemental mapping of C (green), Cu (blue) and O (yellow) images are provided. HR-TEM image of Cu@C-POP-**A** with clear crystalline lattice fringe (c), half exposed Cu NPs wrapped inside the porous channel (d) with lattice fringe (e) for Cu@C-POP-**B**.

The structural detail in depth of Cu@C-POP-**A** and Cu@C-POP-**B** has been further explored extensively by HR-TEM images analysis. The crystalline fringes of a distinct single ~12 nm spherical Cu particle in Cu@C-POP-**A** portrayed in Fig. 3c with the crystalline phase of

Cu(200), resembling with the 0.181 nm *d*-spacing. As shown in Fig. 3d, the ultrathin C-POP carbonaceous layer spread over a micrometre-scale area, revealing the Cu particles are tightly wrapped inside the layer in a half exposed manner. Interestingly, we can recognize a layer for Cu@C-POP-**B** in Fig. 3e, which covered individual metal particles to prohibit the agglomeration, sintering and leaching to improve the catalytic efficiency along with enhanced stability. During the NPs formation process, $NaBH_4$ reduced the metal ion to zero valent metal NPs, then adsorbed on the surface of each NP to provide the stabilization. Most importantly, adsorption of BH_4^- ion on the NP surface generate electrical double layer which emerged on columbic repulsion between individual particles, thus prevents the NPs aggregation as well as restrain NPs diffusion out from the polymer framework.[41] Interestingly, a new discovery about the polymer metal interaction gave a permanent footprint in the formation of chemoselective and long-lived catalysts.[42] Incorporation of metal NPs into to soft polymer framework through dynamic metal-polymer interaction (DMPI) supposed to be the fundamental aspect of emergence of shell outside of Cu nanoparticles in Cu@C-POP-**B**. From Fig. 3e, the crystalline fringe having interplannar *d* spacing of about 0.150 nm literally represents the (220) plane of Cu_2O species.

Porosity and Framework Structure:

Molecular connectivity and chemical environment to different carbon nuclei of the catechol enriched porous-organic-polymer network has been verified by the ^{13}C CP solid state MAS NMR analysis. A strong signal appeared at δ=31.02 ppm in the spectrum, attributed to the methylene ($-CH_2$) linker between the two cathechol moiety (Fig. 4a).[43] The characteristic signals corresponding to the aromatic carbon linked with -OH functional group and the nearest neighbor of that group attached to the methylene linker emerged at δ=145.1 and 138.8 ppm, respectively. A weak distinguishable peak at δ=131.1 ppm, accorded to the unsubstituted sp^2 carbon of the aromatic ring. The existence of carbon atom adjacent to oxygen was noticed at δ=54.1ppm, accountable for the presence of some unreacted FDA molecules.[43] Temperature programmed reduction using H_2 gas (H_2-TPR) is an analytic technique to scrutinize the surface chemistry of metals and metal oxides under different temperature. Previous literature reports reveal the two overlapping peaks from 200^o to 320^{o}C for pure CuO, assigned for the reduction process Cu^{+2} to Cu^0 via Cu^{+1}.[44] In Fig. S8, a broad reduction peak in the region of 200°-450 °C was observed for Cu@C-POP-**A**, indicates the highly dispersed CuO_x phase and large clusters, are in good agreement with previous reports.[46] Interestingly, Cu@C-POP-**B** exhibited lower reduction peak

compared to pure CuO, attributed to the different metal support interaction. A distinct peak located at ~200 °C with a shoulder of 165ºC, indicative to the presence of bulk CuO_x phase and atomically dispersed copper species consist of isolated copper ions, weak magnetic associates as well as small two/three dimensional clusters.[45] From this above mentioned H2-TPR study we can unambiguously demonstrates that such kind of diverse results would reflect on the catalytic activity with the different degree of sintering of nanoparticles, observed from reused catalyst TEM images.

Permanent porosity of the respective materials has been examined by N_2 adsoprtion/desorption analysis at 77 K (Fig. S9). In the low P/P_0 region C-POP exhibited preliminary N_2 uptake subsequently, a slow increase at a relatively intermediate pressure, and a sharp gas uptake at a relatively high pressure with no permanent hysteresis loop, which could be attributed to the existence of hierarchical porous structures comprised of both micropores and mesopores.[47] N_2 sorption profiles could be interpreted as typical combination of type-I and type-IV isotherms according to the IUPAC classification. The shape of N_2-isotherm shape has been nicely preserved for Cu@C-POP-**B** material, in strong contrast Cu@C-POP-**A** yielded a typical type I isotherm with the saturation of N_2 uptake parallel with the relative pressure region, indicating permanent microporous network. The specific (Brunauer-Emmett-Teller) BET surface areas of the C-POP, Cu@C-POP-**A** and Cu@C-POP-**B** materials have been evaluated as 585.8, 315.1 and and 468.4 m^2g^{-1}, respectively, with the corresponding pore volumes 0.391, 0.195 and 0.273 cm^3g^{-1}, respectively. We have observed a diminishment in the BET surface areas owing to the accommodation of Cu-NPs over the porous surface and mass increment of the parent POP, thereby inhibiting N_2 uptake. Our observation is fully consistent with the previous report by Wang *et.al*.[48] The corresponding pore size distributions (Fig. S10) calculated by nonlocal density functional theory modeling (NLDFT), demonstrated that the two respective POPs (C-POP and Cu@C-POP-**B**) display the equivalent broad distribution of mesopores in the range of ~2.3-6.4 nm. A narrow pore size distribution predominately rising in the micropores region (1.45 nm) for Cu@C-POP-**A** material was found.

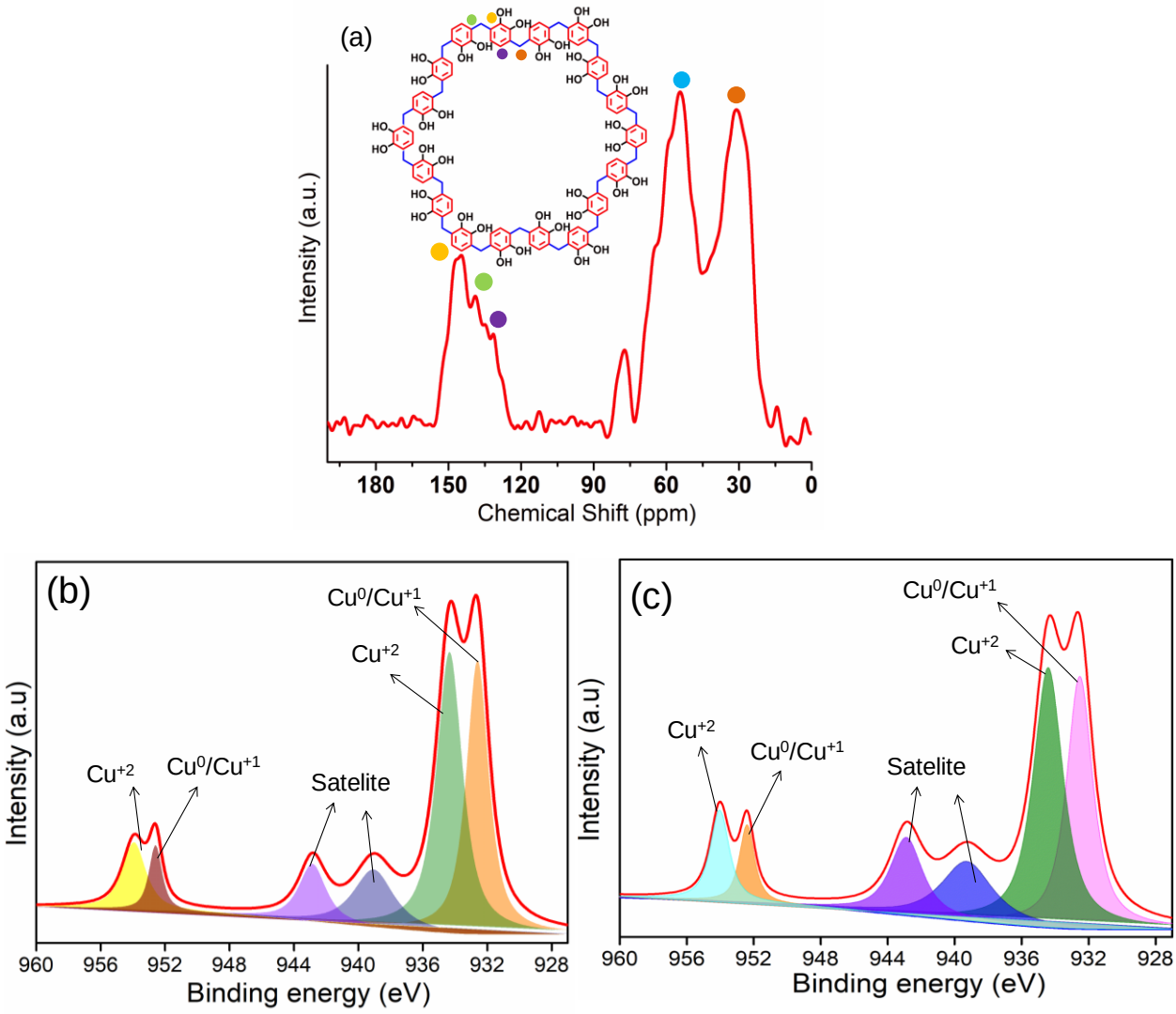

Fig. 4: ^{13}C CP Solid state MAS-NMR spectrum of as-synthesized C-POP (a) and Core-level XP spectra of Cu-2p (b and c), for Cu@C-POP-**A** and Cu@C-POP-**B** materials, respectively.

XPS Analysis:

As illustrated in Fig. S12, the concomitant appearance of C-1s, Cu-2p, O-1s core regions were scrutinized through highly surface sensitive XPS analysis for the respective Cu@C-POP-**A**, Cu@C-POP-**B** catalysts. The XPS result demonstrates the surface elemental composition as well as modification in chemical and electronic state attributed to surface interfacial effects of each element present on the sample. A consecutive series of binding energies in the range of 284.5eV, 285.5-285.7eV, 288.2-288.5eV were distinguished in the C1s XPS spectra (Fig. S13a and 13b), could be attributed to C=C and C-OH, C=O functional groups respectively.[49] A prominent peak shifting in the order of 0.2-0.4 eV, mainly associated with the difference in the synthetic

procedure involved during the reduction period to produce balanced Cu^0 and Cu^{x+} surface species, are in good agreement with previous report.[50] The characteristic binding energy peaks corresponding to Cu-$2p_{3/2}$, Cu-$2p_{1/2}$ for Cu^0 or Cu^{+1} species assigned at ~932.6 eV and ~952.4 eV, respectively (Fig. 4b and 4c) for the both materials.[51] However, we can't define actual oxidation state very precisely by XPS analysis due to overlap of Cu^0 and Cu^{+1} spectra.[51] Cu-$2p_{3/2}$ binding energy peaks located at 934 and 934.4 eV, signifies the existence of Cu^{+2} oxidation state, are in good agreement with the previous report.[52] Herein, a positive binding energy displacement (~0.4eV) for Cu@C-POP-**B** in comparison with Cu@C-POP-**A** is noticed, which could be attributed to the smaller dimension of Cu NPs. Recently, Yamamoto *et al.* reported the peak intensity and displacement of Cu-$2p_{3/2}$ XPS binding energy region played pivotal role on enhancement in ionicity of the Cu-O bonds with the smaller particle size for zirconia supported Cu_nO_x (n = 12, 28, and 60) materials, whereas smallest $Cu_{12}O_x$ materials achieved an excellent catalytic activity in aerobic oxidation of the CH_3 group bonded with aromatic rings.[53] In addition, the corresponding satellite peaks are observed at ~939, ~942.7 eV could be explained as a result of collision of emitted photoelectrons with the valence electrons which are being excited to higher energy levels for the both catalyst, signifies the presence of CuO phase.[54] As a result of this collision, the kinetic energy of the photoelectron decreases, seemed to be the main reason behind the appearance of satellite peak in higher binding energies. The higher satellite peak intensity of CuO for Cu@C-POP-**B** compared with Cu@C-POP-**A**, could be attributed to the feasible reduction of CuO thin layer in presence of hydrogen gas to convert into larger amount metallic Cu^0, which may have the possibility to eventually promoted the catalytic activity.[55] XPS study is a surface sensitive analysis, provide the kinetic energy of the emitted photoelectron, generated within 5 nm of the sample surface, can detect the lower quantity of CuO phase.[55] So, It is in good agreement from the previous report that CuO phase formed on the surface as a very thin layer due to air oxidation during storage or transformation into XPS chamber, only confirmed through highly surface sensitive XPS probe.[56] High resolution deconvoluted O-1s core level XP spectra demonstrates the binding energy peaks situated around 531.6 and 532.8 eV corroborated to C-OH and C-O functional groups, confirming the chemical composition of the Cu-POP integrated system (Fig. S13c and 13d).[57]

XAFS Analysis:

To unearth the status of Cu on the surface and underpin the structure activity relationship we have conducted synchrotron radiation-based X-ray absorption fine structure (XAFS) spectroscopy. Fig. 5a depicts the K-edge X-ray absorption near-edge structure (XANES) spectra of Cu@C-POP based integrated systems with considering the spectra of CuO, Cu_2O and Cu foil as references.[58] The XANES region in the Cu K-edge spectra (Fig. 5a) has characteristic features due to the $1s \rightarrow 4p$ electric dipole allowed transitions. Cu(I) compounds exhibit peak maximum at ~ 8983 eV, while Cu(II) compounds exhibit only a broad low energy tail in the region below 8986 eV. The absorption edge position both the Cu@C-POP-**A** and Cu@C-POP-**B** matches closer to the CuO standard indicating the presence of Cu(II). Additionally, the Cu(I) standard has a relatively intense peak at 8981 eV, which is much reduced in the two catalysts spectra. The variation of the intensity at 8981 eV between the Cu@C-POP-**A** and Cu@C-POP-**B** materials is likely due to presence of a small amount of Cu(0) species in Cu@C-POP-**B**, with the EXAFS (Extended X-ray absorption for fine structure determination) providing more information on this. So from this XANES absorption edge positions we can surely confirm that the Cu species in both the systems in between the valence state of 0 and +2. Jiao *et al*. have reported similar kind of finding in their Cu doped $Pd_{10}Te_3$ nanowires by XANES analysis.[59] The Fourier-transformed k^3-weighted spectra shows the distance of scattersers from the absorbing Cu centre (Fig. 5c). Both samples Cu@C-POP-**A** and Cu@C-POP-**B** have a primary coordination sphere dominated by O, peaks at ~1.94Å (Fig. 5b). These peaks broadly match with the Cu(I) and Cu(II) references in R(Å), with the intensity of CuO being slightly higher. Cu_2O has a peak maximum for first shell Oxygen coordination around 0.1 Å shorter than both the CuO reference and the two samples. As Cu_2O is tetrahedral and 2 coordinate to O and CuO is square planar (with two additional bonds to oxygen at ~ 2.8 Å, see image below), suggesting that the two samples are not tetrahedral in geometry. The Cu foil has a large peak at ~ 2.23 Å due to first shell Cu-Cu metallic bonds, which has a much higher intensity than the Cu-O bonds, which is a consequence of Cu being a heavier scatterer and having a coordination number of 12 (Fig. 6c). Cu@C-POP-**A** exhibits a small peak at ~2.08 Å indicating a low degree of Cu-Cu metallic bonds present. However, Cu@C-POP-**B** does not have a significant scattering contribution at this distance (intensity has been reduced in comparison with Cu@C-POP-**A**), suggesting the Cu first coordination sphere was protected predominately by O atoms only.[60] Also we have noticed a slight shift in the wavelength

transform from 2.23 to 2.08 Å with that of Cu foil, which may be due to the low coordination number (CN) and the contraction of Cu-Cu bond in our Cu@C-POP based integrated system. Both the references CuO and Cu_2O show second shell peaks in the range 2.5-3.5 Å which corresponds to Cu-Cu bond distances in the oxides. The lack of a scattering contribution in this region for the two catalysts Cu@C-POP-**A** and Cu@C-POP-**B** would be consistent with there being no long-range order on average.

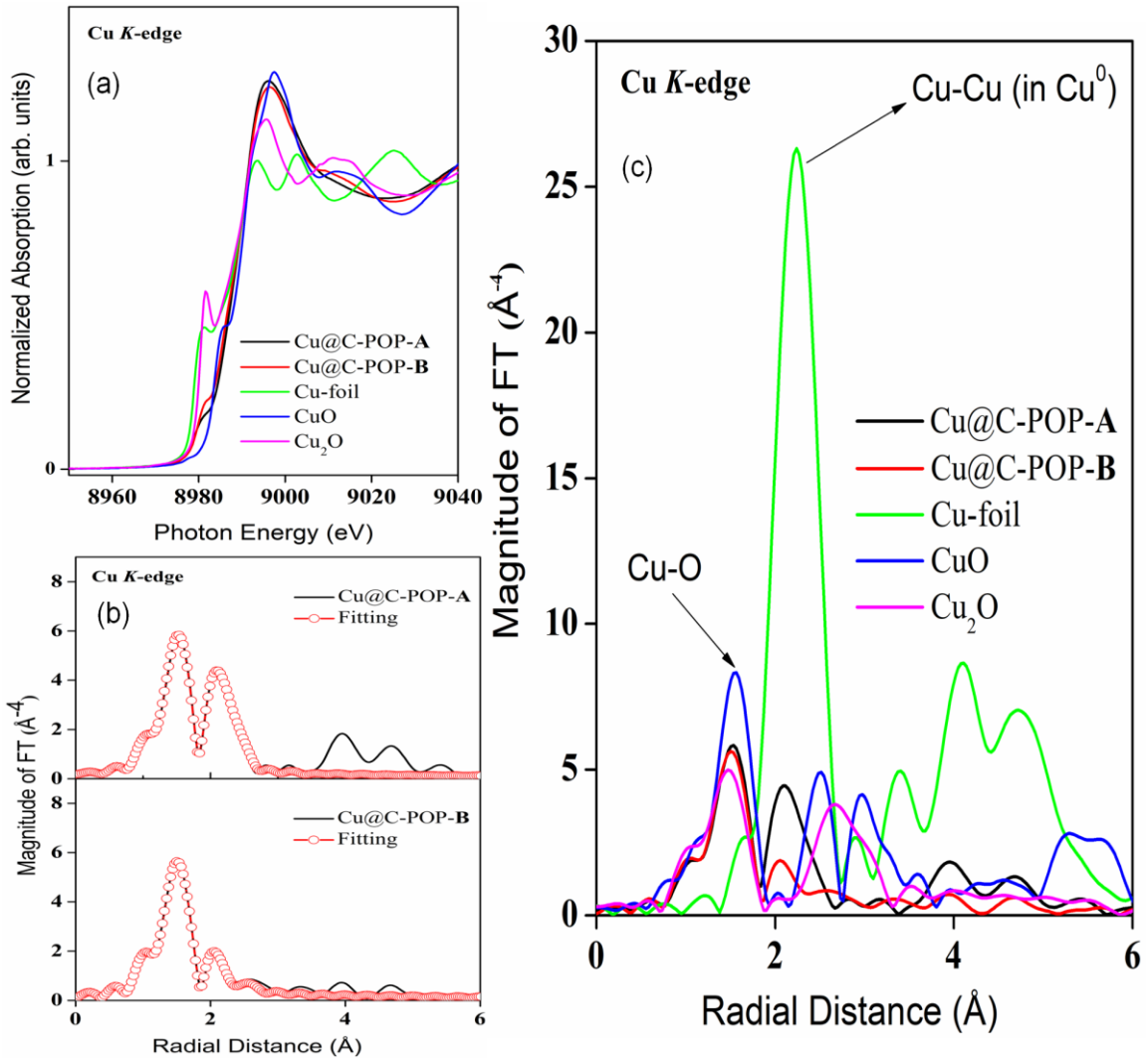

Fig. 5: Normalized (a) Cu K-edge XANES spectra of Cu@C-POP-A, Cu@C-POP-B, Cu Foil, Cu_2O and CuO standard, respectively, (b) Cu K-edge Fitting spectra of the both catalysts, (c)

Fourier transforms of k^3-weighted Cu K-edge and EXAFS spectra of Cu@C-POP-**A**, Cu@C-POP-**B**, Cu Foil, Cu_2O and CuO standard, respectively.

Table 1: Local Structural Results from the First-Shell EXAFS Analysis of the Cu@C-POP based Catalytic Systems

Catalyst	First Shell	CN	R (Å)	DWF ($Å^2$)
Cu@C-POP-**A**	Cu-O	4	1.94	0.0052
	Cu-Cu	2	2.55	0.0073
Cu@C-POP-**B**	Cu-O	3.88	1.93	0.0053
	Cu-Cu	0.85	2.57	0.0089

The local atomic environment and geometrical effect in the Cu@C-POP integrated systems have been evaluated by EXAFS analysis with the fitting results as provided in the Table 1. The first shell coordination number of the Cu@C-POP-**A** is 4, and is what would be expected if two catechol moieties from the POP unit were bonded to the Cu through two hydroxy groups each (Table 1). The bond length of Cu-O for this sample is 1.94 Å, longer than in Cu_2O 1.85 Å (Fig. S14) which has a tetrahedral geometry. CuO has square planar geometry with a first shell Cu-O bond distance of an average of ~ 1.95 Å, with two more Cu-O bonds at 2.78 Å. This longer bond length may be a consequence of weaker Cu-O bonds in the Cu@C-POP samples compared to in Cu_2O. Alternatively this may be due to the Cu having a square planar geometry with respect to the oxygens, which would also have the effect of lengthening the bonds. The Cu@C-POP-**B** sample has a first shell oxygen coordination number of 3.88 and a Cu-Cu coordination number (CN) of 0.88 (Table 1), suggesting that a fraction of Cu is present as mononuclear. This is very close to what was seen in the Cu@C-POP-**A** sample. A small amount Cu(0) clusters would explain this, although it is possible that there is also diatomic Cu species present. Considering the variation in Cu-Cu CNs (Table 1) presented above, From the Table 1, the fitting results unambiguously signifies that the Cu-Cu coordination number is 2 in Cu@C-POP-**A**, much

smaller than that of standard Cu foil (12), which suggests that Cu exists as bicomponent surface species with atomic-level dispersion. Our hypothesis is strongly supported with the appearance of increased amplitudes features between 2.2 and 3.2 Å for Cu@C-POP-**A**, thereby revealing of a heavy backscatter (Cu), in good agreement with the previous report by Lercher and his co-workers in Cu-Oxo dimers stabilized by Zirconia Nodes of an NU-1000 Metal-Organic Framework.[61]

Assessment on Selective performances of 5-HMF hydrogenation of the catalysts:

The selective hydrogenation of 5-HMF to DHMF is a highly appealing route due to its versatile application in ether, ketone, and polymer production industry. To reveal the catalytic reactivity and stability over the Cu@C-POP catalysts, we further investigated the catalytic efficiency of the two respective catalytic systems (Cu@C-POP-**A** and Cu@C-POP-**B**) by performing liquid phase selective hydrogenation of 5-HMF to DHMF. Our present investigation was performed in a 100 ml in a stainless-steel reactor inbuilt with a pressure gauge setup by mixing 30 ml EtOH to 0.126g (1mmol) 5-HMF at 150 °C temperature and 20 bar hydrogen pressure over the respective catalyst (30 mg) for 10 h. The progress of the catalytic reaction with the distribution of reactants and products components in the resulting mixture after the completion of the reaction are determined by GC-FID technique based on authentic sample. Evolution of reactant and product distributions against time (h) of the both catalysts has been displayed in Fig. 6. The reaction was accompanied with a gradual enhancement in DHMF selectivity (16-21%) for both Cu@C-POP-**A** and Cu@C-POP-**B** with negligible amount of side product formation after an initial 4 h, which demonstrates that 5-HMF is mainly selectively hydrogenated to DHMF in the first step. The 5-HMF conversion reached to 33 and 68 % with 90 and 98% DHMF selectivity after 6 h continuous reaction for Cu@C-POP-**A** and Cu@C-POP-**B**, respectively. However, the significant difference in catalytic performance was noticed after 8 h of the reaction where 48 to 95% 5-HMF conversion followed by DHMF selectivity 83 to 100% for the two catalysts Cu@C-POP-**A** and Cu@C-POP-**B**, respectively, have been achieved (Fig. 6a and 6b). Although, the 5-HMF conversion increases gradually as a function of time, the selectivity of DHMF decreases 96 to 87% in the interval of 4 to 10 h accompanied by the formation of unnecessary side products for Cu@C-POP-**A** catalyst. After 12 h a drastic drop in DHMF selectivity from 87 to 68% was noticed for Cu@C-POP-**A** (Fig. 6a). In stark contrast, a steady increase in 5-HMF conversion

with respect to time is observed and DHMF selectivity remains preserved for Cu@C-POP-**B**. Cu@C-POP-**B** exhibits superior catalytic performance in the selective hydrogenation of 5-HMF, providing high conversion (95%) and selectivity (100%) to the desired product DHMF after 8 h. Further continuation of reaction for 12 h would not cause any change in DHMF selectivity Cu@C-POP-**B**. Furthermore, we have investigated the influence of reaction temperature and H_2 pressure on the reactant and product distributions in the selective hydrogenation of 5-HMF over both the catalytic systems (Fig. 7). The decisive role of reaction temperature has been evaluated from our present study by conducting the catalytic hydrogenation reaction at various temperatures (130-170 °C) under 20 bar H_2 pressure. Initially, Cu@C-POP-**A** and Cu@C-POP-**B** respective catalysts furnished 5-HMF conversion (57 and 55%) with DHMF selectivity (71 and 94%) at 130 °C temperature (Fig. 7a and 7b). However, in this case other side products generated with the selectivity of 13 and 6% for Cu@C-POP-**A** and Cu@C-POP-**B**, respectively. Accelerating trends in catalytic activity and more selectivity towards desired product distribution upon raising the temperature from 130 °C to 150 °C for both catalysts have been observed which unambiguously demonstrates much faster reaction kinetics. Despite this catalytic activity enhancement with temperature, a drastic drop in 5-HMF conversion from 88% to 74% and DHMF selectivity from 68% to 42% on Cu@C-POP-**A** was attained on further reaching temperature to 170 °C (Fig. 7a). The activity loss of the catalyst supposed to be effected by several factors including reduction of active species or sintering of NPs at higher temperature, a well-known phenomenon for the diffusion of monomers or small clusters of atoms. The required temperature at which the atoms from the defects & from the bulk became mobile known as Hüttig and Tamman temperatures, respectively ($T_{Hüttig} = 0.3T_{melting}$, $T_{Tamman} = 0.5T_{melting}$), whereas melting point temperature noticed for Cu is 1083 °C. Interestingly, several times it was observed that sintering can occur below Tamman temperature based on various factors including catalyst properties as well as pre treatment/reaction conditions.[62,63] In addition, accumulation of coke or reactant/products over the surface of the active Cu site might be an another factor which accelerated the catalyst deactivation.[64] Similar kind of diminishment trend in DHMF selectivity from 100 to 73% over Cu@C-POP-**B** at 170 °C is also followed (Fig. 7b). This gradual drop in the desired product DHMF selectivity against reaction temperature could be attributed to the partial etherification reaction of 5-HMF with ethanol leading to the production of 5-(ethoxymethyl)furan-2-carbaldehyde (EMF) in the presence of -OH groups functionalized solid

porous catalyst. There are so many reports where it has been clearly confirmed the etherification of HMF in presence of solid acid catalyst. Lanzafame *et al.* reported that presence of lewis acidic site significantly influence the EMF formation by Al-MCM-41 (50) catalyst.[65] The proposed mechanism of formation of EMF was stated that the adsorption of HMF on the lewis acidic site lead to the evolution of oxonium ion, than the further nucleophilic attack by ethanol promote EMF production.[65]In our work, we successfully developed –OH group functionalised porous organic polymer by simple $FeCl_3$ assisted polymerisation reaction between catechol & dimethoxymethane. So, It is quite clear that the presence of OH group are main culprit for formation of EMF as a side product, which finely matched with the recent work.[66] The abovementioned work clearly demonstrated the presence of a weak desorption peak at 170 ^{o}C in NH_3 TPD analysis, due to the lewis acidic site achieved from the hydroxyl group of SBA-15 catalyst. In our work, NH_3 TPD of C-POP reveals the surface acid strength 3.20 mmol/g, clearly demonstrates the strong acidic nature due to the presence large number of –OH group of catechol nonnumeric unit in the polymer framework (Fig. S15). Selective hydrogenation of 5-HMF was consequently screened over different H_2 pressure ranging from 10-30 bar under fixed reaction temperature of 150 °C. Very insignificant 5-HMF conversion (only 2 and 4%) with 100% DHMF selectivity was noticed for both integrated catalytic systems Cu@C-POP-**A** and Cu@C-POP-**B**, respectively, at 10 bar H_2 pressure. Although a progressive result obtained when the 20 bar H_2 pressure was employed in the reaction vessel. In this case, we have achieved 88 and 100% 5-HMF conversion accompanied by 68 and 100% DHMF selectivity for Cu@C-POP-**A** and Cu@C-POP-**B**, respectively (Fig. 7c and 7d). The trend behind the increase in 5-HMF conversion as a function of H_2 pressure, probably due to the elevated dissolved H_2 on the solvent under enhanced hydrogen pressure condition. Although, there is a certain drop in DHMF selectivity from 100% to 47% on Cu@C-POP-**A** and 100% to 86% on Cu@C-POP-**B** at 30 bar H_2 pressure was discovered, corresponding to the increase in other side products selectivity like (5-(ethoxymethyl)furan-2-yl) methanol (EMFM), thereby increasing etherification reaction followed by subsequent hydrogenation reaction under high H_2 pressure.[67] The higher activity of Cu@C-POP-**B** than Cu@C-POP-**A** could be established from N_2O chemisorption results (Table S1) which clearly indicate that Cu@C-POP-**B** exhibited higher active metal surface area (151.92 m^2g^{-1}) accompanied by higher dispersion (22.45% dispersion factor) than Cu@C-POP-**A** catalyst

which showed less active metal surface area (133.99 m^2g^{-1}) along with lower dispersion (19.8% dispersion factor).

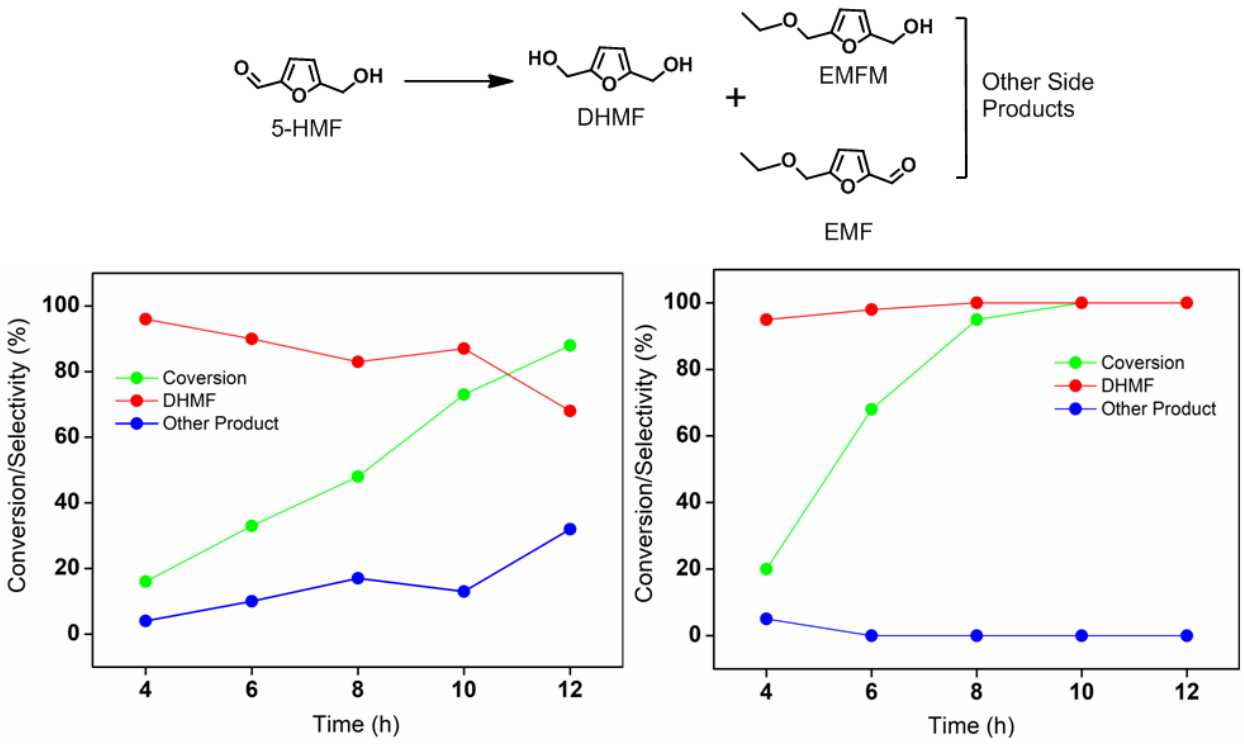

Fig. 6: Evolution of reactant and product distributions as a function of time (a and b) for Cu@C-POP-**A** and Cu@C-POP-**B**, respectively. Reaction conditions: HMF (1 mmol, 126 mg), EtOH (30 mL), catalyst (30 mg), H_2 pressure (20 bar), temperature (150 °C), time (10 h).

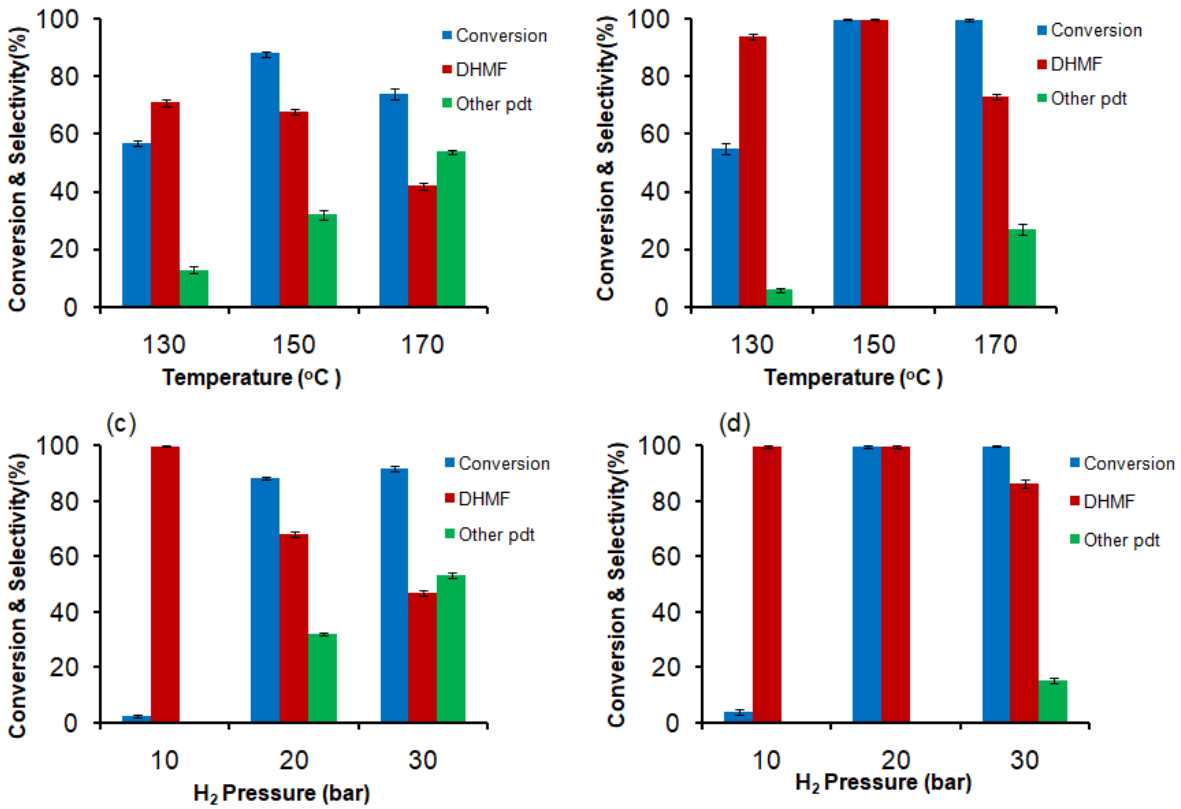

Fig. 7: Influence of reaction temperature (a and b) and H_2 pressure (c and d) the reactant and product distributions for Cu@C-POP-**A** and Cu@C-POP-**B**, respectively. Reaction conditions: HMF (1 mmol, 126 mg), EtOH (30 mL), catalyst (30 mg), H_2 pressure (20 bar), temperature (150 °C), time (10 h).

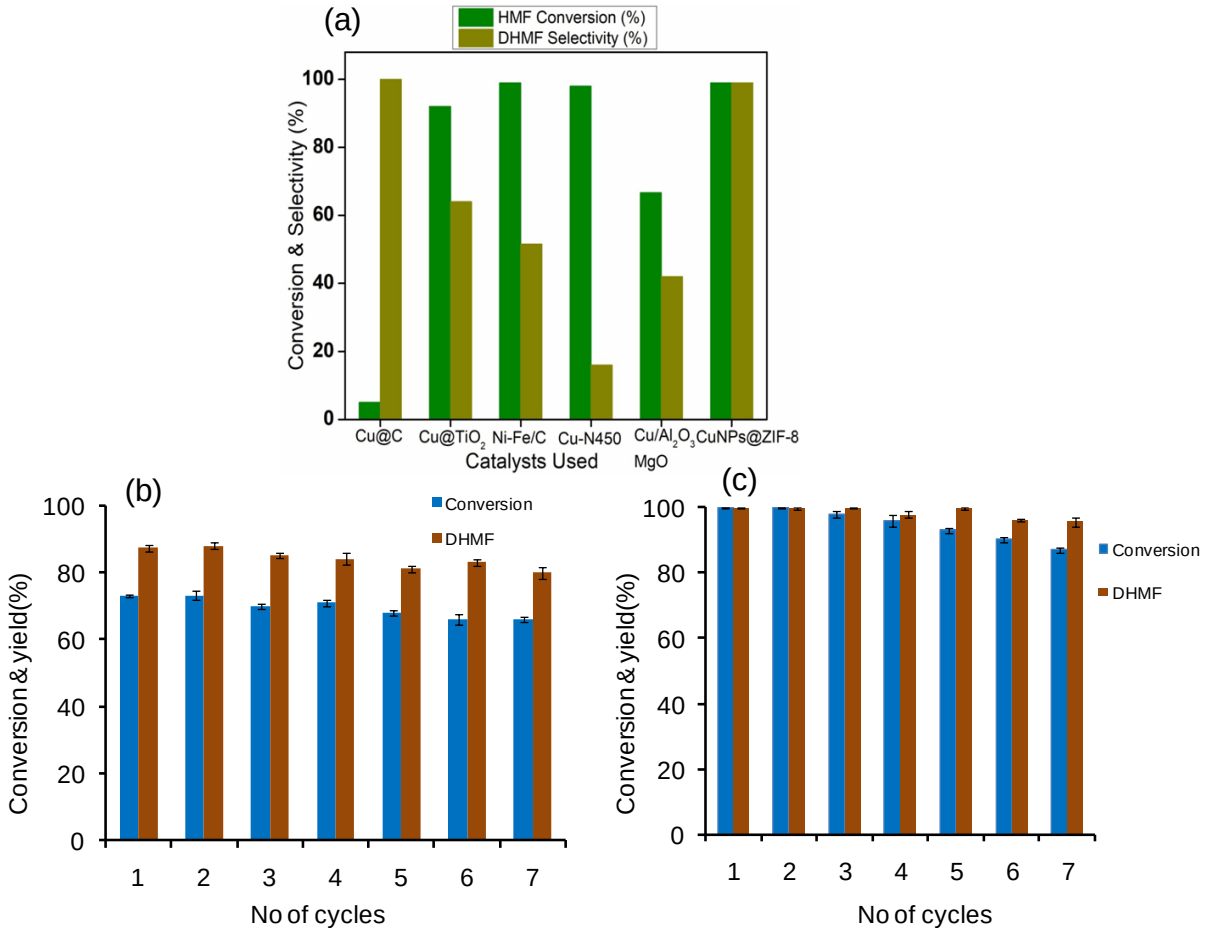

Fig. 8: (a) Catalytic activity of screened and the reference catalysts, reusability test of Cu@C-POP-**A** (b) and Cu@C-POP-**B** (c) respectively. Reaction conditions: HMF (5 mmol, 630 mg), EtOH (150 mL), catalyst (200 mg), H_2 pressure (20 bar), temperature (150 ºC), time (10 h).

We have also envisaged the selective hydrogenation of HMF over commercially available support like C and TiO_2 by comparing with the recently reported Cu-based catalyst on Fig. 8. The carbon supported Cu catalyst appeared to be inert compared to TiO_2 based catalyst with the 5% and 92 % 5-HMF conversion followed by 100%, 64% of DHMF selectivity under optimized condition. Xu *et al.* recently reported MOF derived bimetallic catalyst Ni-Fe/C with 99% 5-HMF conversion and 51.6 % DHMF selectivity at 140^{o}C, under 2MPa H_2 pressure.[13] Interestingly, the synergistic effect between Cu^{+1} and Cu^{0} played the crucial role for the activity of Cu-N450 catalyst with 98% 5-HMF conversion followed by very poor DHMF selectivity(16%).[16] One of the most recently observed fact was demonstrated by Hu *et al.*, reveals the introduction of alkaline additives to the monometallic Cu/Al_2O_3 will readily increase the catalytic hydrogenation

of 5-HMF at lower temperature.[12] Cu/Al_2O_3MgO catalyst showed the superior catalytic activity with the 66.7% 5-HMF conversion and 42% DHMF selectivity compared to Cu/Al_2O_3 catalyst (7.5% con, 1.9% sel).[12] The excellent catalytic activity over selective hydrogenation of 5-HMF (99% con) to DHMF (99% sel) formation was obtained by CuNPs@ZIF8 catalyst composed of highly active bicomponent Cu^1-Cu^0 species.[16] The comparison study with various reported catalysts for Hydrogenation of 5-HMF to DHMF, provided on Table S2, clearly demonstrated the higher catalytic activity of our Cu@C-POP-**B** catalysts. Reusability test of the respective Cu@C-POP-**A** and Cu@C-POP-**B** catalysts were accomplished to investigate the inherent stability under optimized reaction condition up-to seven consecutive catalytic runs (Fig. 8b and 8c). After each catalytic cycle the catalyst was separated from the reaction mixture by simple centrifugation technique, washed with MeOH (3-4 times) followed by drying in oven at 80 °C and subsequently reused for the next catalytic run. Cu@C-POP-**B** exhibited excellent recyclability without a significant drop in 5-HMF conversion and with the marginal drop of DHMF selectivity from 100% to 87% after seventh catalytic cycle. In strong contrast, a significant drop in 5-HMF conversion from 73% to 66% for Cu@C-POP-**A** catalyst was noticed which could be ascribed to the polymerization of 5-HMF during thermal condition over the catalyst external surface, thus blocking the accessible active sites.[37] ICP-OES result also indicates the consistent structural integrity through a negligible amount of Cu wt% loss for Cu@C-POP-**B** during the reaction (Cu loading of fresh and reused catalyst are 1.63 and 1.58 $mmolg^{-1}$), whereas more significant drop in Cu wt% from 1.35 to 1.23 $mmolg^{-1}$ compare to Cu@C-POP-**B** specified the poor stability of the Cu@C-POP-**A**. The intrinsic stability of Cu@C-POP-**B** catalyst is likely to be explained with the synthetic procedure involved ($NaBH_4$ reduction method) where an electrical double layer is generated between individual particles columbic repulsion force, thus the uncontrollable growth of metal particles and particle aggregation were suppressed.[68] In order to make certain our new developed catalyst is indeed heterogeneous in nature, hot-filtration test of the catalyst was also performed. After 6 h of reaction time, the catalyst (especially here Cu@C-POP-**B**) was isolated from the hot reaction mixture, where 65% 5-HMF conversion was attained at this point, as confirmed by GC-MS analysis. The reaction was further continued with the filtrate for another additional 8 h at the same reaction temperature but no improvement in conversion was observed, as confirmed by GC-MS analysis, which distinctly reveals the limited leaching of Cu metal nanoparticles in the

reaction mixture has been restricted owing to the carbon layer of the POP framework protection and tight wrapping (Fig. S17). After 24 h of the catalytic reaction we observed a light blue color, probably some homogeneous Cu leaching below 2 ppm level as determined by AAS (Atomic Absorption Spectroscopy) analysis, caused by the inevitable intergranular friction, followed by collision with the stirrer and autoclave wall under the constant vigorous stirring conditions. In order to check whether homogeneous leached Cu species into the filtrate is active or not we have introduced excess 5-HMF and conducted the reaction under optimized reaction conditions for about 24 h. However, only 2-3% product conversion was obtained after 24 h, which proved that leached Cu species did not catalyze this reaction. TEM images of the respective used catalysts Cu@C-POP-**A** and Cu@C-POP-**B** after 7^{th} catalytic run demonstrated on Fig. S19. The recombination of two nearby spheres during the catalysis process on Cu@C-POP-**A** lead to the formation of parrot head like morphology on Fig. S19a. Spheres morphology clearly indicates the structure almost remain unaltered with insignificant amount of sphere overlap even after seven consecutive catalytic run (Fig. S19b). Surface reconstruction as well as reshaping of metal NPs over the POP surface induced the transformation original sphere to square accompanied by reduced homogeneous dispersion NPs over the porous surface, appeared after exposure of the supported metal particles of Cu@C-POP-**B** catalyst to the reactive environment. Overlapping nature of the individual squares instigated the formation of irregular shapes shown on Fig. S19d. Although the structural integrity of the two catalysts was compromised to a small extent, the two catalysts showed a marginal drop in 5-HMF conversion and DHMF selectivity up to 7^{th} catalytic run. To determine the oxidation state of elements present in the re-used catalyst after the reactions XPS analysis was performed. The deconvoluted XPS spectra of Cu-2p for both the catalyst represented in Fig. S20a and S20b. Two decisive binding energy peaks corresponds to Cu^{+2} at ~934.07 eV and ~953.8 eV was observed in core-level spectra for Cu@C-POP-**A** catalyst, including the satellite peaks at ~ 940.2 eV and ~943.1 eV indicating the chemical composition of the catalyst was sustained. Another characteristic binding energy peak corresponds to Cu-$2p_{3/2}$ was observed at ~933 eV indicating the presents of Cu^0 species in the catalyst surface which explains the unaltered catalytic activity for Cu@C-POP-**A** even after the 7^{th} catalytic cycle. However, in case of Cu@C-POP-**B** the XPS spectra show some alteration comparing with the fresh catalyst. Characteristic binding energy peaks at ~934 eV and ~953.9 eV along with the satellite peaks at ~940.5 eV and ~943.7 eV assigned to Cu^{+2} in the catalyst

surface. But one of the crucial binding energy peak corresponds to Cu^0 species was missing indicating the absence of Cu^0 NPs in the surface which may be due to the leaching and aggregation of Cu NPs onto the surface forming larger particles, which can be clearly seen from the TEM images Fig. S19c and S19d. Due to the aggregation of Cu NPs after 7^{th} catalytic cycle explains the decline in the catalytic activity of the Cu@C-POP-**B** compare to the fresh catalyst.

Density Functional Theory studies were performed to explain the observed difference in catalytic activity towards DHMF formation over the Cu@C-POP-**A** and Cu@C-POP-**B** catalysts. The characterization results suggest Cu to be presented in an oxidation state between 0 and +2, with a strong presence of CuO on both catalyst surfaces. It is interesting to note that the Cu-Cu coordination number decreased from 2 for Cu@C-POP-**A** to 0.88 for the Cu@C-POP-**B** catalyst. Note that the desired catalytic activity is provided by the surface Cu atoms which have a smaller coordination number compared to the inner bulk atoms. To model the Cu@C-POP-**A** and Cu@C-POP-**B** catalyst, the most stable facet of CuO(111) was chosen. The surface Cu atom of CuO(111) is coordinated to two other surface Cu atoms in line with the observed EXAFS results. To mimic the observed decrease in Cu-Cu coordination number, the Cu@C-POP-**B** catalyst was modelled by creating a Cu vacancy on the CuO(111) surface by removing a surface Cu atom a Cu(111) vac surface (see Fig. 9). This process would reduce the local surface Cu-Cu coordination number to 1. The presence of a Cu vacancy shifts the lattice O atoms in its immediate vicinity by around 0.4 to 0.7 Ǻ relative to their initial lattice positions. Although, similar defect surfaces of CuO(111) have been explored for the design of effective photoelectrodes for the solar to chemical energy conversions, the effect of Cu metal vacancies on catalytic activity remains largely unexplored. Fig. 9 illustrates the most stable adsorption configurations of HMF and DHMF along with their binding energies on CuO(111) and CuO(111)_vac surfaces. The HMF molecule binds via the formyl oxygen on the CuO(111) surface in a slightly tilted configuration with the furan ring away from the surface. Furfural derivatives have been reported to bind in a η^1 (-O) orientation on Cu surfaces.[69] A binding energy of -117 kJ/mol and -121 kJ/mol was calculated on the CuO(111) and CuO(111)_vac surfaces respectively, which is in reasonable agreement with previously reported values.[70]

The conversion of HMF to DHMF proceeds via a 2 step sequential hydrogenation of the formyl group of HMF. The reaction energy profile is shown in Fig. 10. The first hydrogenation step can

either occur at the O or C end of the formyl group to give rise to F-CHOH or F-CH_2O species respectively (where F denotes the furan ring). Our calculations show that the F-CHOH species is significantly more stable than the F-CH_2O species on both the model surfaces. The formyl carbon of F-CHOH binds to the surface O with a C-O bond distance of 1.5 and 1.48 Å on the CuO(111) and CuO(111)_vac surfaces respectively. A similar interaction is however absent for the F-CH_2O species. In addition, the F-CHOH species binds 112 kJ/mol stronger on the CuO(111)_vac surface relative to the defect free CuO surface. This is not surprising as the presence of a vacancy leads to an enhanced electron density on the CuO surface, which results in a higher ability to bind to adsorbate molecules. HMF hydrogenation to F-CHOH proceeds with a barrier of 77 and 117 kJ/mol on the CuO(111)_vac and CuO(111) surface respectively. The significantly lower formyl O hydrogenation barriers on the defect CuO surface can explain the observed higher catalytic activity on the Cu@C-POP-**B** catalyst. In contrast, the second hydrogenation at the formyl C end to form DHMF had a higher barrier of 256 kJ/mol on the CuO(111)_vac, compared to 230 kJ/mol for the CuO(111) surface. However, note that the overall activation barrier for DHMF starting from an adsorbed HMF, is only 199 kJ/mol on the CuO(111)_vac surface compared to 281 kJ/mol for CuO(111) surface. Our DFT calculations hence indicate HMF hydrogenation to DHMF to be kinetically favorable on the CuO(111)_vac surface – which resembles the synthesized Cu@C-POP-**B** catalyst.

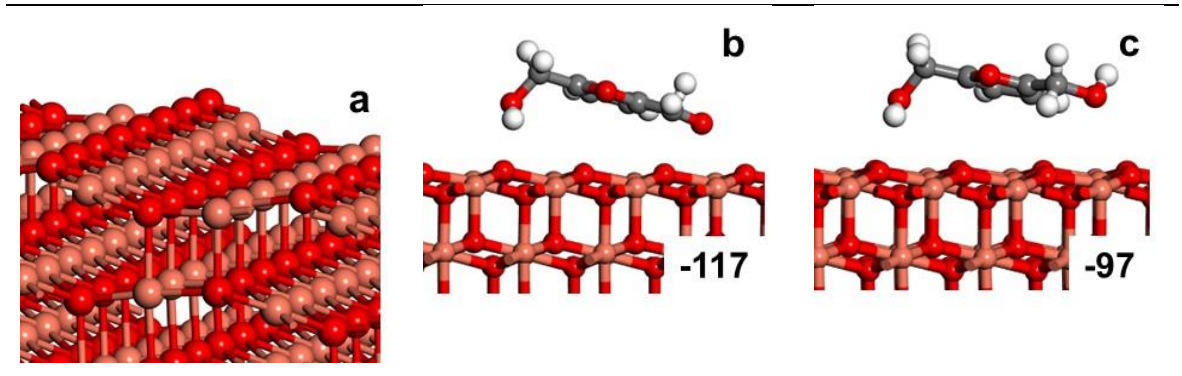

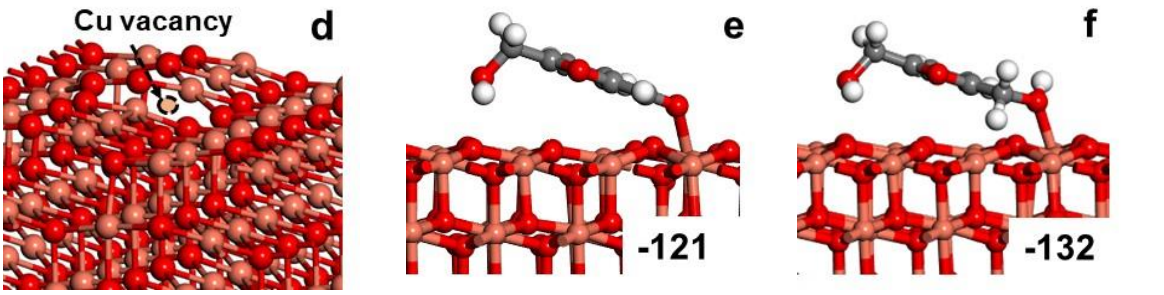

Fig. 9: Adsorption configurations and binding energies of 5-HMF and DHMF on CuO(111) and CuO(111)_vac surfaces. a) CuO(111) surface; b) 5-HMF on CuO(111); c) DHMF on CuO(111); e) 5-HMF on CuO(111)_vac; f) DHMF on CuO(111).

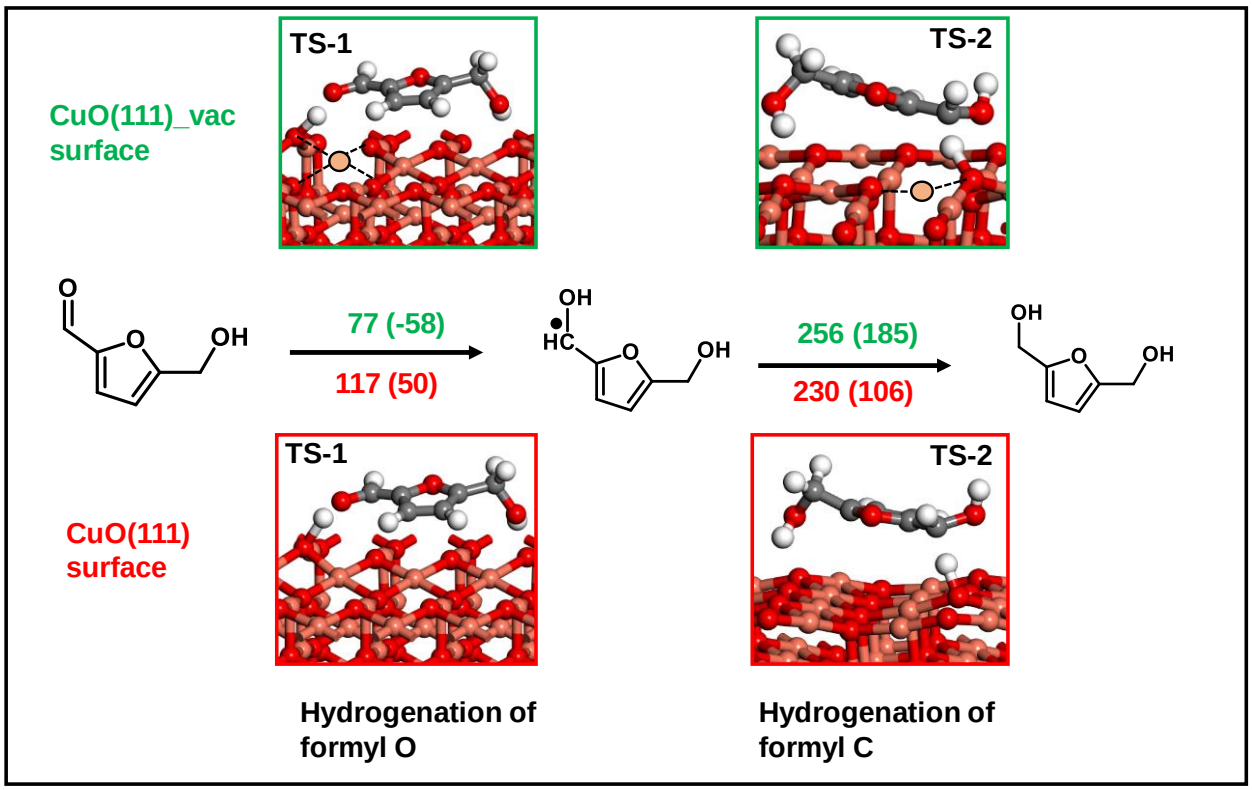

Fig. 10: Schematic illustrating the reaction energy profile for hydrogenation of 5-HMF to DHMF on CuO(111) and CuO(111)_vac surfaces. The activation barriers and reaction energies (in parenthesis) are indicated in kJ/mol. The Cu vacancy site on the CuO(111)_vac is also indicated.

Conclusion:

In this work, a new method has been introduced to synthesize catechol based Porous-Organic-Polymer (POP) supported Cu based catalysts (Cu@C-POP-**A** and Cu@C-POP-**B**) with coexisting Cu^0 and Cu^{x+} active species inside the nanocage of POP framework for selective hydrogenation of 5-HMF to DHMF. Comparatively, Cu@C-POP-**B** exhibit higher catalytic

activity affording 98% DHMF selectivity at 150°C temperature and 20 bar H_2 pressure. The interconnection of structure and activity of the synthesized catalysts was established through various in-depth characterization technique and DFT analysis. H_2-TPR and XPS analysis of Cu@C-POP-**B** nanohybrid indicate the presence of atomically dispersed copper species consist of isolated copper ions as well as bulk CuO_x phase with the positive binding energy shifts (0.4 eV) of Cu $2p_{3/2}$ spectra for the smaller dimension of Cu NPs. In addition, EXAFS analysis of Cu@C-POP-**B** reveals the presence of Cu vacancies on the CuO surface which eventually modulate the coordination number Cu, lead to decrease the coordination number of first shell Cu-O and Cu-Cu bond to 3.88 and 0.88 and consequently helps in increment of activity of the catalyst. Density Functional Theory calculations further shed light on the reaction mechanism and clearly indicates that the existence of Cu vacancies stabilized the transition state and lowered the energy barriers by 40 kJ/mol which facilitates the selective hydrogenation of 5-HMF to DHMF–a well known monomer in polymer industry. We believe that the distinguishable porous layer trapped the smaller Cu NPs during the reduction process which not only shields them from oxidation and deactivation, but also prevent leaching and agglomeration of Cu-NPs up to 7^{th} catalytic run, which distinctly manifested a promising route to generate exceptionally stable heterogeneous catalyst for hydrogenation 5-HMF to DHMF, important feedstock of resin and artificial fiber industry.

Associated Content:

Supporting Information

The Supporting Information is available free of charge on the ACS Publications website. Characterization Techniques, Thermo gravimetric analysis (TGA), intermolecular H bonding between catechol layers, FE-SEM images, TEM images & SAED patterns, EDX patterns, Wide angle powder X-ray diffraction pattern, H_2-TPR study, N_2-adsorption/desorption isotherms, Pore size distributions (NLDFT method), FT-IR spectra, XP survey spectra, Core-level XP spectra of C-1s and O-1s, Coordination geometry, NH_3-TPD analysis, N_2O chemisorptions Study, catalyst leaching text, GC-MS data, reused catalysts TEM images, XPS spectra, Comparison Study with various reported catalysts.

❖ Authors Information:

Corresponding Authors

*E-mail for J.M.: johnmondal@iict.res.in; johncuchem@gmail.com

*E-mail for A.B.: arghyab@iitrpr.ac.in

Authors Contributions

[Δ]C.S. and R.P have equally contributed.

Notes

The authors declare no competing financial interest.

❖ Acknowledgements:

C.S. and R.P. wish to thankfully acknowledge the Council of Scientific and Industrial Research (CSIR)-University grant commission (UGC), New Delhi, and the DST-INSPIRE (GAP-0799) for their respective senior research fellowships. J.M. is very much grateful acknowledges the Department of Science and Technology, India, for the DST-INSPIRE Faculty Research project grant (GAP-0522), CSIR-YSA Research Grant (Reference no: HRDG/YSA-19/02/21(0045)/2019) & Focused Basic Research (FBR) Grant under CLP theme (reference no. 34/1/TD-CLP/NCP-FBR 2020-RPPBDD-TMD-SeMI) for financial support at CSIR-IICT, Hyderabad. We sincerely thank Director, CSIR-IICT (Ms. No. IICT/Pubs./2020/346.) for providing all the required facilities to carry out the work.

REFERENCES:

1. Singuru, R.; Dhanalaxmi, K.; Shit, S. C.; Reddy, B. M.; Mondal, J. Palladium Nanoparticles Encaged in a Nitrogen-Rich Porous Organic Polymer: Constructing a Promising Robust Nanoarchitecture for Catalytic Biofuel Upgrading. *ChemCatChem* **2017**, *9*, 2550-2564; DOI: 10.1002/cctc.201700186.

2. Shit, S. C.; Koley, P.; Joseph, B.; Marini, C.; Nakka, L.; Tardio, J.; Mondal, J. Porous Organic Polymer-Driven Evolution of High-Performance Cobalt Phosphide Hybrid Nanosheets as Vanillin Hydrodeoxygenation Catalyst. *ACS Appl. Mater. Interfaces* **2019**, *11*, 24140-24153; DOI: 10.1021/acsami.9b06789.

3. Koley, P.; Shit, S. C.; Joseph, B.; Pollastri, S.; Sabri, Y. M.; Mayes, E. L. H.; Nakka, L.; Tardio, J.; Mondal, J. Leveraging Cu/$CuFe_2O_4$-Catalyzed Biomass-Derived Furfural

Hydrodeoxygenation: A Nanoscale Metal–Organic-Framework Template Is the Prime Key. *ACS Appl. Mater. Interfaces* **2020**, *12*, 21682-21700; DOI: 10.1021/acsami.0c03683.

4. Shit, S. C.; Singuru, R.; Pollastri, S.; Joseph, B.; Rao, B.S.; Lingaiah, N.; Mondal, J. Cu-Pd Bimetallic Nanoalloy Anchored on a N-rich Porous Organic Polymer for High-Performance Hydrodeoxygenation of Biomass-derived Vanillin. *Catal. Sci. Technol.* **2018**, *8*, 2195-2210; DOI: 10.1039/C8CY00325D.

5. Paul, R.; Sarkar, C.; Yan, Y.; Trinh, Q. T.; Rao, B. S.; Pao, C. W.; Lee, J. F.; Liu, W.; Mondal, J. Porous-Organic-Polymer-Triggered Advancement of Sustainable Magnetic Efficient Catalyst for Chemoselective Hydrogenation of Cinnamaldehyde. *ChemCatChem* **2020**, *12*, 3687-3704; DOI: 10.1002/cctc.202000072.

6. Sarkar, C.; Shit, S. C.; Dao, D. Q.; Lee, J.; Tran, N. H.; Singuru, R.; An, K.; Nguyen, D. N.; Le, Q. V.; Amaniampong, P. N.; Drif, A.; Jerome, F.; Huyen, P. T.; Phan, T. T. N.; Vo, D.-V. N.; Thanh Binh, N.; Trinh, Q. T.; Sherburne, M. P.; Mondal, J. An Efficient Hydrogenation Catalytic Model Hosted in a Stable Hyper-Crosslinked Porous-Organic-Polymer: from Fatty Acid to Bio-Based Alkane Diesel Synthesis. *Green Chem.* **2020**, *22*, 2049-2068; DOI:10.1039/C9GC03803E.

7. Chen, J.; Liu, R.; Guo, Y.; Chen, L.; Gao, H. Selective Hydrogenation of Biomass-Based 5-Hydroxymethylfurfural over Catalyst of Palladium Immobilized on Amine-Functionalized Metal–Organic Frameworks. *ACS Catal.* **2015**, *5*, 722-733; DOI: 10.1021/cs5012926.

8. Mitra, J.; Zhou, X.; Rauchfuss, T. Pd/C-Catalyzed Reactions of HMF: Decarbonylation, Hydrogenation, and Hydrogenolysis. *Green Chem.* **2015**, *17*, 307-313; DOI: 10.1039/C4GC01520G.

9. Alamillo, R.; Tucker, M.; Chia, M.; Pagán-Torres, Y.; Dumesic, J. The Selective Hydrogenation of Biomass-Derived 5-Hydroxymethylfurfural Using Heterogeneous Catalysts. *Green Chem.* **2012**, *14*, 1413–1419; DOI: 10.1039/C2GC35039D.

10. Ohyama, J.; Esaki, A.; Yamamoto, Y.; Araic, S.; Satsuma, A. Selective Hydrogenation of 2-Hydroxymethyl-5-Furfural to 2,5-Bis(hydroxymethyl)furan over Gold Sub-nano Clusters. *RSC Adv.* **2013**, *3*, 1033-1036; DOI: 10.1039/C2RA22190J.

11. Yin, A.; Guo, X.; Dai, W. L.; Fan, K. The Nature of Active Copper Species in Cu-HMS Catalyst for Hydrogenation of Dimethyl Oxalate to Ethylene Glycol: New Insights on the Synergetic Effect between Cu^0 and Cu^+. *J. Phys. Chem. C.* **2009**, *113*,11003-11013; DOI: 10.1021/jp902688b.

12. Sun, K.; Shao, Y.; Li, Q.; Liu, Q.; Wu, W.; Wang, Y.; Hu, S.; Xiang, J.; Liu, Q.; Hu, X. Cu-Based Catalysts for Hydrogenation of 5-Hydroxymethylfurfural:Understanding of the Coordination Between Copper and Alkali/alkaline Earth Additives. *Mol Catal.* **2019**, *474*, 110407; DOI: 10.1016/j.mcat.2019.110407.

13. Zhang, S.; Ma, H.; Sun, Y.; Luo, Y.; Liu, Y.; Zhang, M.; Gao, J.; Xu, J. Catalytic Selective Hydrogenation and Rearrangement of 5-Hydroxymethylfurfural to 3-Hydroxymethyl-cyclopentone Over a Bimetallic Nickel-Copper Catalyst in Water. *Green Chem.* **2019**, *21*, 1702–1709; DOI: 10.1039/C8GC04009E.

14. Zhu, Y.; Kong, X.; Zheng, H.; Ding, G.; Zhu, Y.; Li, Y. W. Efficient Synthesis of 2,5-Dihydroxymethylfuran and 2,5-Dimethylfuran from 5-Hydroxymethylfurfural Using Mineral-Derived Cu Catalysts as Versatile Catalysts. *Catal. Sci. Technol*. **2015**, *5*, 4208-4217; DOI: 10.1039/C5CY00700C.

15. Feng, Y.; Yan, G.; Wang, T.; Jia, W.; Zeng, X.; Sperry, J.; Sun, Y.; Tang, X.; Lei, T.; Lin, L. Cu^{1}-Cu^{0} Bicomponent CuNPs@ZIF-8 for High-Selective Hydrogenation of Biomass Derived 5-Hydroxymethylfurfural. *Green Chem.* **2019**, *21*, 4319-4323; DOI: 10.1039/C9GC01331H.

16. Zhang, Q.; Zuo, J.; Peng, F.; Chen, S.; Wang, Q.; Liu, Z. A Non-Noble Monometallic Catalyst Derived from Cu–MOFs for Highly Selective Hydrogenation of 5-Hydroxymethylfurfural to 2,5-Dimethylfuran. *ChemistrySelect* **2019**, *4*, 13517-13524; DOI: 10.1002/slct.201903256.

17. Yue, H.; Zhao, Y.; Zhao, S.; Wang, B.; Ma, X.; Gong, J. A Copper-phyllosilicate Core-sheath Nanoreactor for Carbon-Oxygen Hydrogenolysis Reactions. *Nat. Commun.***2013**, *4*, 2339; DOI:10.1038/ncomms3339

18. Shit, S. C.; Khilari, S.; Mondal, I.; Pradhan, D.; Mondal, J. The Design of a New Cobalt Sulfide Nanoparticle Implanted Porous Organic Polymer Nanohybrid as a Smart and Durable Water-Splitting Photoelectrocatalyst. *Chemistry A European Journal* 2017, *23*, 14827-14838; DOI: 10.1002/chem.201702561.

19. Shit, S. C.; Shown, I.; Paul, R.; Chen, K. H.; Mondal, J.; Chen, L. C. Integrated Nano-architectured Photocatalysts for Photochemical CO_2 Reduction. *Nanoscale* **2020**, *12*, 23301-23332; DOI: 10.1039/D0NR05884J.

20. Paul, R.; Shit, S. C.; Fovanna, T.; Ferri, D.; Rao, B. S.; Gunasooriya, G. T. K. K.; Dao, D. Q.; Le, Q. V.; Shown, I.; Sherburne, M. P.; Q. T.; Mondal, J.; Realizing Catalytic Acetophenone Hydrodeoxygenation with Palladium-Equipped Porous Organic Polymers. *ACS Appl. Mater. Interfaces* **2020**, *12*, 50550-50565; DOI: 10.1021/acsami.0c16680.

21. Kresse, G.; Furthmuller, J. Efficient Iterative Schemes for ab Initio Total-Energy Calculations Using a Plane-wave Basis Set. *Phys. Rev. B: Condens. Matter Mater. Phys.* **1996**, *54*, 11169; DOI: 10.1103/PhysRevB.54.11169.

22. Dion, M.; Rydberg, H.; Schroder, E.; Langreth, D. C.; Lundqvist, B. I. Van der Waals Density Functional for General Geometries. *Phys. Rev. Lett.* **2004**, *92*, 246401; DOI: 10.1103/PhysRevLett.92.246401.

23. Mohan, O.; Trinh, Q. T.; Banerjee, A.; Mushrif, S. Predicting CO_2 Adsorption and Reactivity on Transition Metal Surfaces Using Popular Density Functional Theory Methods. *Mol Simul*. **2019**, *45:14-15*, 1163-1172; DOI: 10.1080/08927022.2019.1632448

24. Dudarev, S. L.; Botton, G. A.; Savrasov, S. Y.; Humphreys, C. J.; Sutton, A. P. Electron-Energy-Loss Spectra and the Structural Stability of Nickel Oxide: An LSDA+U Study. *Phys. Rev. B.* **1998**, *57*, 1505-1509; DOI: 10.1103/PhysRevB.57.1505.

25. Trinh, Q. T.; Bhola, K.; Amaniampong, P. N.; Jeró ̂me, F.; Mushrif, S. H. Synergistic Application of XPS and DFT to Investigate Metal Oxide Surface Catalysis. *J. Phys. Chem. C* **2018**, *122*, 22397−22406; DOI: 10.1021/acs.jpcc.8b05499.

26. Mills, G.; Jonsson, H. Quantum and thermal effects in H_2 dissociative adsorption: Evaluation of Free Energy Barriers in Multidimensional Quantum Systems. *Phys. Rev. Lett*. **1994**, *72*, 1124-1127; DOI: 10.1103/PhysRevLett.72.1124.

27. Modak, A.; Bhanja, P.; Bhaumik, A. Microporous Nanotubes and Nanospheres with Iron-Catechol Sites: Efficient Lewis Acid Catalyst and Support for Ag Nanoparticles in CO_2 Fixation Reaction. *Chem. Eur. J.* **2018**, *24*, 14189-14197; DOI: 10.1002/chem.201802319.

28. Baty, A. M.; Leavitt, P. K.; Siedlecki, C. A.; Tyler, B. J.; Suci, P. A.; Marchant, R.; Geesey, G. G. Adsorption of Adhesive Proteins from the Marine Mussel, *Mytilus edulis*, on Polymer Films in the Hydrated State Using Angle Dependent X-ray Photoelectron Spectroscopy and Atomic Force Microscopy. *Langmuir* **1997**, *13*, 5702-5710; DOI: 10.1021/la9610720.

29. Schnurrer, J.; Lehr, C. M. Mucoadhesive Properties of the Mussel Adhesive Protein. *Int. J. Pharm.* **1996**,*141*, 251-256; DOI: 10.1016/0378-5173(96)04625-X.

30. Lu, Q.; Oh, D. X.; Lee, Y.; Jho, Y.; Hwang, D. S.; Zeng, H. Nanomechanics of Cation–π Interactions in Aqueous Solution. *Angew Chem. Int. Ed.* **2013**, *52*, 3944-3948; DOI: 10.1002/anie.201210365.

31. Patil, N.; Jrôme, C.; Detrembleur, C. Recent Advances in the Synthesis of Catechol-derived (Bio)polymers for Applications in Energy Storage and Environment. *Prog. Polym. Sci.* **2018**, *82*, 34-91; DOI:10.1016/j.progpolymsci.2018.04.002.

32. Dawson, R.; Stevens, L. A.; Drage, T. C.; Snape, C. E.; Smith, M. W.; Adams, D. J.; Cooper, A. I. Impact of Water Coadsorption for Carbon Dioxide Capture in Microporous Polymer Sorbents. *J. Am. Chem. Soc.* **2012**, *134*, 10741-10744; DOI: 10.1021/ja301926h.

33. Mondal, S.; Singuru, R.; Shit, S. C.; Hayashi, T.; Irle, S.; Hijikata, Y.; Mondal, J.; Bhaumik, A. Ruthenium Nanoparticle-Decorated Porous Organic Network for Direct Hydrodeoxygenation of Long-Chain Fatty Acids to Alkanes. *ACS Sustainable Chem. Eng.* **2018**, *6*, 1610-1619; DOI: 10.1021/acssuschemeng.7b02772.

34. Ma, X.; Sun, Z.; Su, W.; Yi, Z.; Cui, X.; Guo, B.; Li, X. Biologically Inspired, Catechol-Coordinated, Hierarchical Organization of Raspberry-like Calcium Phosphate Nanospheres with High Specific Surface Area. *J. Mater. Chem. B* **2018,** *6*, 3811-3819; DOI: 10.1039/C7TB03156D.

35. Ling, P.; Hao, Q.; Lei, J.; Ju, H. Porphyrin Functionalized Porous Carbon Derived from Metal-Organic Framework as a Biomimetic Catalyst for Electrochemical Biosensing. *J. Mater. Chem. B.* **2015**, *3*, 1335-1341; DOI: 10.1039/C4TB01620C.

36. Giannousi, K.; Avramidis, I.; D. -Samara, C. Synthesis, Characterization and Evaluation of Copper Based Nanoparticles as Agrochemicals Against Phytophthora Infestans. *RSC Adv.* **2013**, *3*, 21743-21752; DOI: 10.1039/C3RA42118J.

37. Chen, L.; Zhang, Y.; Zhu, P.; Zhou, F.; Zeng, W.; Lu, D. D.; Sun, R.; Wong, C. Copper Salts Mediated Morphological Transformation of Cu_2O from Cubes to Hierarchical Flower-like or Microspheres and Their Supercapacitors Performances. *Sci. Rep.* **2015**, *5*, 9672; DOI: 10.1038/srep09672.

38. Alsawafta, M.; Badilescu, S.; Packirisamy, M.; Truong, V. V. Kinetics at the Nanoscale: Formation and Aqueous Oxidation of Copper Nanoparticles. *Reac Kinet Mech Cat* **2011**, *104*, 437-450; DOI: 10.1007/s11144-011-0352-x.

39. Liu, Q. M.; Zhou, D. b.; Yamamoto, Y.; Ichino, R.; Okido, M. Preparation of Cu Nanoparticles with $NaBH_4$ by Aqueous Reduction Method. *Trans. Nonferrous Met. Soc. China* **2012**, *22*, 117-123; DOI: 10.1016/S1003-6326(11)61149-7.

40. Khan, A.; Rashid, A.; Younas, R.; Chong, R. A Chemical Reduction Approach to the Synthesis of Copper Nanoparticles. *Int Nano Lett* **2016**, *6*, 21-26; DOI:10.1007/s40089-015-0163-6.

41. Sarkar, C.; Pendem, S.; Shrotri, A.; Dao, D. Q.; Pham Thi Mai, P.; Nguyen Ngoc, T.; Mondal, J. Interface Engineering of Graphene Supported Cu Nanoparticles Encapsulated by Mesoporous Silica for Size-Dependent Catalytic Oxidative Coupling of Aromatic Amines. *ACS Appl. Mater. Interfaces* **2019**, *11*, 11722-11735; DOI: 10.1021/acsami.8b18675.

42. Lee, S.; Shin, S. J.; Baek, H.; Choi, Y.; Hyun, K.; Seo, M.; Kim, K.; Koh, D. Y.; Kim, H.; Choi, M. Dynamic Metal-polymer Interaction for the Design of Chemoselective and Long-lived Hydrogenation Catalysts. *Sci. Adv.* **2020**, *6*, eabb7369; DOI: 10.1126/sciadv.abb7369

43. Breller, S.; Liang, H. W.; Kramm, U. I.; Krumpfer, J. W.; Feng, X. L.; Muellen, K. Bimetallic Porous Porphyrin Polymer-derived Non-precious Metal Electrocatalysts for Oxygen Reduction Reactions. *J. Mater. Chem. A.* **2015**, *3*, 23799-23808; DOI: 10.1039/C5TA06309D.

44. Ding, S.; Xu, M.; Hu, J.; Xiao, W.; Cai, J.; Zhang, N. Porous Organic Polymer-Templated Porous Copper-Ceria with Highly Dispersed Copper Oxide and Excellent Activity for CO Oxidation. *Catal. Letters.* **2019**, *149*, 322-327; DOI: 10.1007/s10562-018-2605-z.

45. Dow, W. P.; Wang, Y. P.; Huang, T. J. TPR and XRD Studies of Yttria-doped Ceria/g-Alumina-Supported Copper Oxide Catalyst. *Appl Catal A: Gen.* **2000**, *190*, 25-34; DOI: 10.1016/S0926-860X(99)00286-0.

46. Tian, H.; Zhang, X. L.; Scott, J.; Ng, C.; Amal, R. TiO_2-supported Copper Nanoparticles Prepared *via* Ion Exchange for Photocatalytic Hydrogen Production. *J. Mater. Chem. A.* **2014**, *2*, 6432-6438; DOI: 10.1039/C3TA15254E.

47. Huang, W.; Gu, C.; Wang, T.; Gu, C.; Qiao, S.; Yang, R. Effect of Two Facile Synthetic Strategies with Alterable Polymerization Sequence on the Performance of N-Vinyl Carbazole-based Conjugated Porous Materials. *RSC Adv.* **2014**, *4*, 62525-62531; DOI: 10.1039/C4RA11611A.

48. Cui, C.; Tang, Y.; Ziaee, M. A.; Tian, D.; Wang, R. Highly Dispersed Ultrafine Palladium Nanoparticles Enabled by Functionalized Porous Organic Polymer for Additive-Free Dehydrogenation of Formic Acid. *ChemCatChem* **2018**, *10*, 1431-1437; DOI: 10.1002/cctc.201701805.

49. Xu, Z.; Ye, H.; Li, H.; Xu, Y.; Wang, C.; Yin, J.; Zhu, H. Enhanced Lithium Ion Storage Performance of Tannic Acid in LiTFSI Electrolyte. *ACS Omega.* **2017**, *2*, 1273-1278; DOI: 10.1021/acsomega.6b00504.

50. Dave, K.; Park, K. H.; Dhayal, M. Two-step Process for Programmable Removal of Oxygen Functionalities of Graphene Oxide: Functional, Structural and Electrical Characteristics. *RSC Adv*. **2015**, *5*, 95657-95665; DOI: 10.1039/C5RA18880F.

51. Wu, C. K.; Yin, M.; O'Brien, S.; Koberstein, J. T. Quantitative Analysis of Copper Oxide Nanoparticle Composition and Structure by X-ray Photoelectron Spectroscopy. *Chem. Mater.* **2006**, *18*, 6054-6058; DOI: 10.1021/cm061596d.

52. Gao, D.; Zhang, J.; Zhu, J.; Qi, J.; Zhang, Z.; Sui, W.; Shi, H.; Xue, D. Vacancy-Mediated Magnetism in Pure Copper Oxide Nanoparticles. *Nanoscale Res Lett.* **2010**, *5*, 769-772; DOI: 10.1007/s11671-010-9555-8.

53. Sonobe, K.; Tanabe, M.; Yamamoto, K. Enhanced Catalytic Performance of Subnano Copper Oxide Particles. *ACS Nano.* **2020**, *14*, 1804-1810; DOI: 10.1021/acsnano.9b07582.

54. Wang, Z.; Al-Jawhari, H. A.; Nayak, P. K.; Caraveo-Frescas, J. A.; Wei, N.; Hedhili, M. N.; Alshareef, H. N. Low Temperature Processed Complementary Metal Oxide Semiconductor (CMOS) Device by Oxidation Effect from Capping Layer. *Sci. Rep.* **2015**, *9617*, 5; DOI: 10.1038/srep09617.

55. Sarkar, C.; Koley, P.; Shown, I.; Lee, J.; Liao, Y. F.; An, K.; Tardio, J.; Nakka, L.; Chen, K. H.; Mondal, J. Integration of Interfacial and Alloy Effects to Modulate Catalytic Performance of Metal−Organic-Framework-Derived Cu-Pd Nanocrystals toward Hydrogenolysis of 2,5-Hydroxymethylfurfural. *ACS Sustainable Chem. Eng.* **2019**, *7*, 10349-10362; DOI: 10.1021/acssuschemeng.9b00350.

56. Li, Q.; Li, M.; Zhang, S.; Liu, X.; Zhu, X.; Ge, Q.; Wang, H. Tuning Sn-Cu Catalysis for Electrochemical Reduction of CO_2 on Partially Reduced Oxides SnO_x-CuO_x-Modified Cu Electrodes. *Catalysts*. **2019**, *9*, 476; DOI: 10.3390/catal9050476.

57. Diez, N.; Sliwak, A.; Gryglewicz, S.; Grzyb, B.; Gryglewicz, G. Enhanced Reduction of Graphene Oxide by High Pressure Hydrothermal Treatment. *RSC Adv.* **2015**, *5*, 81831-81837; DOI: 10.1039/C5RA14461B.

58. Xiao, H.; Goddard III, W. A.; Cheng, T.; Liu, Y. Cu Metal Embedded in Oxidized Matrix Catalyst to Promote CO_2 activation and CO Dimerization for Electrochemical Reduction of CO_2. *Proc. Natl Acad. Sci. USA*, **2017**, *114*, 6685-6688; DOI: 10.1073/pnas.1702405114.

59. , J.; Lin, R.; Liu, S.; Cheong, W.; Zhang, C.; Chen, Z.; Pan, Y.; Tang, J.; Wu, K.; Hung, S.; Chen, H. M.; Zheng, L.; Lu, Q.; Yang, X.; Xu, B.; Xiao, H.; Li, J.; Wang, D.; Peng, Q.; Chen, C.; Li, Y. Copper Atom-pair Catalyst Anchored on Alloy Nanowires for Selective and Efficient Electrochemical Reduction of CO_2. *Nat. Chem.* **2019**, *11*, 222-228; DOI:10.1038/s41557-018-0201-x.

60. Frenkel, A. I.; Wang, Q.; Marinkovic, N.; Chen, J. G.; Barrio, L.; Si, R.; Cámara, A. L.; Estrella, A. M.; Rodriguez, J. A.; Hanson, J. C. Combining X-ray Absorption and X-ray Diffraction Techniques for in Situ Studies of Chemical Transformations in Heterogeneous Catalysis: Advantages and Limitations. *J. Phys. Chem. C*. **2011**, *115*, 17884-17890; DOI: 10.1021/jp205204e.

61. Zheng, J.; Ye, J.; Ortuño, M. A.; Fulton, J. L.; Gutierrez, O. Y.; Camaioni, D. M.; Motkuri, R. K.; Li, Z.; Webber, T. E.; Mehdi, B. L.; Browning, N. D.; Penn, R. L.; Farha, O. K.; Hupp, J. T.; Truhlar, D. G.; Cramer, C. J.; Lercher, J. A. Selective Methane Oxidation to Methanol on Cu-Oxo Dimers Stabilized by Zirconia Nodes of an NU-1000 Metal−Organic Framework. *J. Am. Chem. Soc*. **2019**, *141*, 9292-9304; DOI: 10.1021/jacs.9b02902.

62. Bartholomew, C. H. Sintering Kinetics of Supported Metals: New Perspectives from a Unifying GPLE Treatment. *Appl Catal A*. **1993**,*107*, 1-57; DOI: 10.1016/0926-860X(93)85114-5.

63. Natesakhawat, S.; Ohodnicki Jr, P.R.; Howard, B. H.; Lekse, J. W.; Baltrus, J. P.; Matranga, C. Adsorption and Deactivation Characteristics of Cu/ZnO-Based Catalysts for Methanol Synthesis from Carbon Dioxide. *Top Catal.* **2013**, *56*, 1752-1763; DOI: 10.1007/s11244-013-0111-5.

64. Liu, D.; Zemlyanov, D.; Wua, T.; Lobo-Lapidus, R. J.; Dumesic, J. A.; Miller, J. T, Marshall, C. L. Deactivation Mechanistic Studies of Copper Chromite Catalyst for Selective Hydrogenation of 2-Furfuraldehyde. *J. Catal.* **2013**, *299*, 336-345; DOI: 10.1016/j.jcat.2012.10.026.

65. Lanzafame, P.; Temi, D.M., Perathoner, S.; Centi, G.; Macario, A.; Aloise, A.; Giordano, G. Etherification of 5-Hydroxymethyl-2-Furfural (HMF) with Ethanol to Biodiesel Components using Mesoporous Solid Acidic Catalysts. *Catal. Today* **2011**,*175*, 435-441; DOI: 10.1016/j.cattod.2011.05.008.

66. Rao, B. S.; Lakshmi, D. D.; Kumari, P. K.; Rajitha, P.; Lingaiah, N. Dehydrative Etherification of Carbohydrates to 5-Ethoxymethylfurfural over SBA-15-Supported Sn-Modified Heteropolysilicate Catalysts. *Sustain. Energy Fuels,* **2020**, *4*, 3428-3437; DOI: 10.1039/D0SE00509F.

67. Wang, Z.; Chen, Q. Conversion of 5-Hydroxymethylfurfural into 5-Ethoxymethylfurfural and Ethyl Levulinate Catalyzed by MOF-based Heteropolyacid Materials. *Green Chem.* **2016**, *18*, 5884-5889; DOI: 10.1039/C6GC01206J.

68. Agnihotri, S.; Mukherji, S.; Mukherji, S. Size-controlled Silver Nanoparticles Synthesized over the Range 5-100 nm using the Same Protocol and their Antibacterial Efficacy. *RSC Adv.* **2014**, *4*, 3974-3983; DOI: 10.1039/C3RA44507K.

69. Shi, Y.; Zhu, Y.; Yang, Y.; Li, Y. W.; Jiao, H. Exploring Furfural Catalytic Conversion on Cu(111) from Computation. *ACS Catal.* **2015**, *5* (7), 4020-4032; DOI: 10.1021/acscatal.5b00303.

70. Ren, J.; Song, K. H.; Li, Z.; Wang, Q.; Li, J.; Wang, Y.; Li, D.; Kim, C. K. Activation of Formyl C-H and Hydroxyl O-H Bonds in HMF by the CuO(111) and Co_3O_4(110) Surfaces: A DFT Study. *Appl. Surf. Sci*. **2018**, *456*, 174-183; DOI: 10.1016/j.apsusc.2018.06.120.

Graphical Abstract:

Navigating Copper-Atom-Pair Structural Effect inside Porous-Organic-Polymer Cavity for Selective Hydrogenation of Biomass Derived 5-Hydroxymethylfurfural

Modulating the balance of Cu^0/Cu^{x+} active species over the catechol based Porous-Organic-Polymer for the selective hydrogenation of biomass-derived 5-Hydroxymethylfurfural to 2,5-dihydroxymethylfuran.